

See discussions, stats, and author profiles for this publication at: <https://www.researchgate.net/publication/380186371>

Releasing long bubbles trapped in thin capillaries via tube centrifugation and inclination

Preprint · July 2024

DOI: 10.48550/arXiv.2404.17934

CITATIONS
0

READS
120

6 authors, including:



Pier Giuseppe Ledda
Università degli studi di Cagliari

40 PUBLICATIONS 201 CITATIONS

[SEE PROFILE](#)



Francois Gallaire
École Polytechnique Fédérale de Lausanne

249 PUBLICATIONS 5,824 CITATIONS

[SEE PROFILE](#)



Ludovic Keiser
CNRS

31 PUBLICATIONS 474 CITATIONS

[SEE PROFILE](#)

Banner appropriate to article type will appear here in typeset article

1 Releasing long bubbles trapped in thin capillaries 2 via tube centrifugation and inclination

**3 Alice Marcotte¹, Pier Giuseppe Ledda², Valentin Buriasco³, Paul Dené³, François
4 Gallaire³, Ludovic Keiser⁴**

5 Institut Jean le Rond d'Alembert, Sorbonne Université, Paris, France,

6 Dipartimento di Ingegneria Civile, Ambientale e Architettura, Università degli Studi di Cagliari, Cagliari,
7 Italy,

8 Laboratory of Fluid Mechanics and Instabilities, École Polytechnique Fédérale de Lausanne, Lausanne,
9 Switzerland,

10 Institut de Physique de Nice, Université Côte d'Azur, Nice, France

11 (Received xx; revised xx; accepted xx)

12 In confined systems, the entrapment of a gas volume with an equivalent spherical diameter
13 greater than the dimension of the channel can form extended bubbles that obstruct fluid
14 circuits and compromise performance. Notably, in sealed vertical tubes, buoyant long bubbles
15 cannot rise if the inner tube radius is below a critical value near the capillary length. This
16 critical threshold for steady ascent is determined by geometric constraints related to the
17 matching of the upper cap shape with the lubricating film surrounding the elongated part
18 of the bubble. Developing strategies to overcome this threshold and release stuck bubbles
19 is essential for applications involving narrow liquid channels. Effective strategies involve
20 modifying the matching conditions with an external force field to facilitate bubble ascent.
21 However, it's unclear how changes in acceleration conditions affect the motion onset of
22 buoyancy-driven long bubbles.

23 This study investigates the mobility of elongated bubbles in sealed tubes with an inner
24 radius near the critical value inhibiting bubble motion in a vertical setting. Two strategies are
25 explored to tune bubble motion, leveraging variations in axial and transversal accelerations:
26 tube rotation around its axis and tube inclination relative to gravity. By revising the
27 geometrical constraints of the simple vertical setting, the study predicts new thresholds
28 based on rotational speed and tilt angle, respectively, providing forecasts for the bubble rising
29 velocity under modified apparent gravity. Experimental measurements of motion threshold
30 and rising velocity compare well with theoretical developments, thus suggesting practical
31 approaches to control and tune bubble motion in confined environments.

32 1. Introduction

33 Air entrapment into liquid-filled channels is encountered in a broad range of applications,
34 from simple hydraulic systems for intravenous filling (Groell *et al.* 1997) to CO₂ sequestration
35 in depleted geological oil reservoirs (Oldenburg & Lewicki 2006; Corapcioglu *et al.* 2004;
36 Wang & Clarens 2012), embolism in circulatory biological systems (Brodribb *et al.* 2016;
37 Li *et al.* 2021), and multiphase microfluidics flows (Baroud *et al.* 2010). In miniaturized

38 fluid systems, air bubbles can be exploited for transport of particles or for mixing processes
 39 (Baroud *et al.* 2007, 2010; Stone *et al.* 2004). Conversely, long gas bubbles may represent a
 40 challenging issue, since they can occlude the entire cross-section of the channel and reduce
 41 the performance of the fluid circuit (Jensen *et al.* 2004; van Steijn *et al.* 2008; Brodribb *et al.*
 42 2016).

43 In application fields involving narrow liquid channels, long bubbles may be challenging
 44 to eliminate, while disrupting fluid flow, causing pressure fluctuations and affecting mixing
 45 processes. In perfusion systems for cell cultures, these bubbles can have several detrimental
 46 effects on cell health and experimental outcomes, such as localized nutrient deprivation,
 47 altered pH levels, and accumulation of waste products, all of which can negatively impact
 48 cell viability and function (Sung & Schuler 2009). As an additional example, in fuel cells, the
 49 oxidation of methanol leads to the formation of CO₂ bubbles, that reduce the cell's efficiency
 50 (Litterst *et al.* 2006). Thus, a considerable effort has been dedicated to the removal of bubbles
 51 in these circuits (see among others Sung & Schuler (2009), Cheng & Lu (2014), Guo *et al.*
 52 (2022)).

53 Conversely, transport of long bubbles in microfluidic channels can be cleverly exploited,
 54 for instance for particle sieving. Since the bubble speed is intrinsically linked to the thickness
 55 of its surrounding lubricating film (Fairbrother & Stubbs 1935), tuning the velocity of the
 56 bubble may be used to separate particles based on their size (Yu *et al.* 2018): monitoring the
 57 speed of the bubble may prevent particles larger than the film thickness to reach the fluid
 58 region past the bubble. The bubble thus acts as an active filter that has the high advantage
 59 of preventing clogging. Thus, enabling and controlling the motion of elongated bubbles in
 60 capillaries can enhance the efficiency of these microfluidic systems.

61 Many hydraulic and microfluidic systems rely on vertical settings (see, for instance, Kaigala
 62 *et al.* 2011), thereby calling for a better understanding of how bubble transport is influenced by
 63 gravity forces. In a vertical configuration, a gas volume in a liquid-filled channel is expected
 64 to rise owing to buoyancy. The more specific case of buoyant ascent in a vertical tube of a
 65 gas volume with an equivalent spherical diameter larger than the tube inner radius, has been
 66 investigated by Dumitrescu (1943) and Davies & Taylor (1950), that provided a prediction for
 67 the rising velocity of long bubbles in tubes, subsequently termed as Taylor bubbles. However,
 68 it was observed over a century ago (Gibson 1913) that long bubbles within a sealed vertical
 69 tube with a sufficiently narrow diameter exhibit an interesting behavior: they cease to rise
 70 and appear to be stuck. This observation was puzzling considering the existence of a thin
 71 lubricating film surrounding long bubbles in tubes, allowing for the drainage of the fluid and
 72 thus for the rising of the bubble. Bretherton (1961) showed that if the tube inner radius was
 73 smaller than a critical value R_c close to the capillary length ℓ_c of the liquid (more precisely,
 74 $R_c \approx 0.918\ell_c$), no valid bubble shape was compatible with a steady rising motion. This
 75 threshold stems from the asymptotic matching between the upper cap profile, which results
 76 from the equilibrium between surface tension and gravity, and the thin film surrounding the
 77 elongated part of the bubble, where viscous, surface tension and gravity forces are balanced.
 78 These two regions are depicted in Figure 1(a). The condition for the onset of motion can
 79 be summarized as a geometrical constraint which imposes, for the existence of a steadily
 80 ascending bubble, that the upper cap profile exhibits an inflection point with negative slope
 81 (for an upward oriented vertical axis), see Figure 1(b). At the critical condition $R = R_c$,
 82 both the slope and curvature vanish at the solid wall. In addition, for R slightly larger than
 83 R_c , Bretherton (1961) predicted the bubble rising velocity, by exploiting mass conservation
 84 through the thin film and the variation of the slope at the inflection point with the tube's
 85 radius.

86 Below the threshold $R < R_c$, Lamstaes & Eggers (2017) studied the unsteady bubble
 87 motion and predicted the occurrence of a self-similar pinch-off singularity of the thin

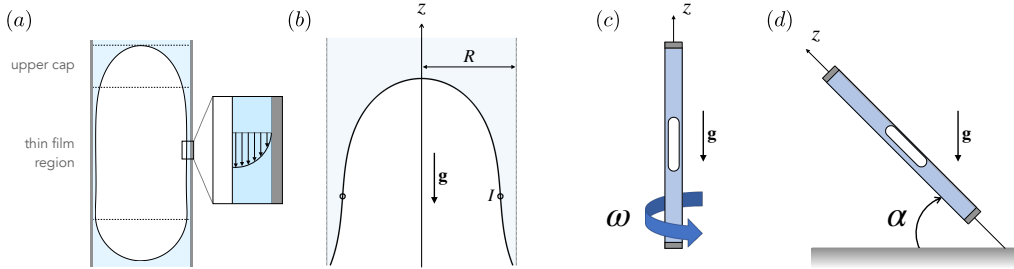


Figure 1: (a) Schematics of a long bubble immersed in a viscous liquid inside a sealed capillary. The top part of the bubble can be divided into an upper cap and into an elongated part surrounded by a thin film. For a buoyant bubble to rise, mass conservation requires the fluid displaced by the tip of the bubble to drain through the thin film. (b) Sketch of the upper cap profile of a long air bubble within a sealed tube of radius R , in the vertical setting studied by Bretherton (1961). The profile exhibits an inflection point denoted by I . For $R > R_c$, the matching with the thin film region at the inflection point is possible. (c) and (d) Sketch of the configurations investigated in this study. In the first case (c), the tube is hold vertically and rotates around its symmetry axis at angular frequency ω . In the second case (d), the tube is tilted with respect to gravity and makes an angle α with the horizontal plane.

88 lubricating film around the bubble, thus hindering any further flow and eventually stopping the
89 progression of the bubble, found to travel a finite distance over infinite time. That prediction
90 is supported by recent interference microscopy experiments, that have demonstrated that the
91 bubble is apparently stuck by an infinitely slow flow taking place in the surrounding thin
92 liquid film whose nanometric thickness results from an equilibrium between capillary stress
93 and disjoining pressure (Dhaouadi & Kolinski 2019).

94 For bubble ascent in sealed tubes, it is necessary for the fluid displaced by the tip of the bubble
95 to drain through the thin film. Thus, enabling the motion of the bubble in sealed tubes
96 with inner radii smaller than the critical value R_c , requires to develop some strategies that
97 would act on the thickness of the surrounding lubricating film. Zhou & Prosperetti (2021)
98 showed numerically that "engaging" the bubble by means of thin vertical rods regularly
99 arranged on a circle coaxial with the tube could effectively expand the gap between the
100 air-liquid interface and the inner solid wall, thus facilitating the downward flow of the liquid
101 and increasing the rising velocity of the bubble. Bi & Zhao (2001) and Bico & Quéré (2002)
102 demonstrated that using angular tubes could effectively promote the rising of the bubble even
103 under strong confinement, owing to the presence of corners that allow for a more efficient
104 drainage of the liquid around the bubble (Funada *et al.* 2005). In the same spirit, another
105 strategy consists in using textured inner walls: because of the imbibition of the roughness,
106 the effective thickness of the lubricating film is actually larger than on a smooth surface (Bico
107 *et al.* 2001).

108 However, in some applications where the geometry of the tube cannot be modified
109 adequately, the film thickness could be varied by adjusting the pressure distribution in
110 the surrounding liquid by mean of an external force field, which could be easily tuned so
111 as to precisely control the ascent velocity of the bubble. In this context, it has been shown
112 that imposing a liquid flow in the tube effectively thickens the lubricating film around the
113 bubble (Yu *et al.* 2021). In particular, Magnini *et al.* (2019) demonstrated that when the
114 external flow is oriented in the same (upward) direction as buoyancy, it can enable the rise
115 of bubbles in tubes with radius $R < R_c$. Kubie (2000) documented a significant increase
116 in the ascent velocity of a Taylor bubble enclosed in a vertical tube subjected to horizontal
117 oscillations. In the case of a vertically oscillated tube, Brannock & Kubie (1996) reported

instead experimental evidences of the slowing down of the bubble, while Madani *et al.* (2009, 2012) observed a more nuanced behavior: as the acceleration of the oscillations is gradually increased, the rising of the bubble initially slows down, but then increases at larger accelerations. More recently, Zhou & Prosperetti (2024) studied the rising behavior of a Taylor bubble exhibiting volume oscillations imposed either by forcing the liquid column above the bubble to oscillate or by imposing a pulsating pressure field at the top liquid surface. Their numerical simulations evidence that the gas volume oscillations result in the thinning of the lubricating film around the bubble and thus in the decrease of the drainage flow and rising velocity.

Here, we focus on the transport of long bubbles in sealed tubes filled with a viscous liquid, with an inner radius close to the critical value below which the bubble is stopped in a vertical configuration. We investigate two different strategies to enable bubble motion and tune its velocity, namely rotating the tube around its symmetry axis, and inclining it with respect to gravity (Figure 1(c) and (d)). In both cases, we leverage theoretical developments to predict the new threshold for the onset of motion, that depends on the rotational speed and on the tilt angle, respectively. We also provide a prediction for the rising velocity of the bubble as a function of the liquid properties, the tube geometry and the (modified) gravity field. Our theoretical findings are then compared with the outcomes of dedicated experimental campaigns.

The paper is organized in two parts. In the first part (Section 2), we report our investigation on bubble motion in rotating tubes. Section 2.1 develops the theoretical prediction for the cap profile of the bubble and the matching conditions between this cap and the flat film region, from which we derive the theoretical threshold for the onset of motion and the prediction of the bubble velocity, in terms of the rotational speed. Section 2.2 presents the experimental setup and a comparison of the results against the theoretical findings. The second part (Section 3) presents the same structure as the previous one, but investigates the effect of tube inclination, with theoretical predictions and comparison with experimental measurements of bubble transport in tilted tubes.

146

147 2. Effect of centrifugation

148 Fluid centrifugation pertains to extensive applications, ranging from the segregation of
 149 complex or biological fluids (Svedberg & Fåhraeus 1926) to numerous industrial processes,
 150 such as wastewater treatment (Turano *et al.* 2002) or crude oil refining (Gary *et al.* 2007).
 151 In interfacial flows, spinning rods (Than *et al.* 1988) and spin-coating (Emslie *et al.* 1958),
 152 are used to deposit uniform thin films onto diverse substrates such as optical lenses for anti-
 153 reflective properties (Krogman *et al.* 2005), or silicon wafers for organic semiconductors
 154 fabrication (Yuan *et al.* 2014). This method precisely controls the film thickness through the
 155 modulation of the angular velocity, essential for achieving high-quality coatings. Additionally,
 156 centrifugation can be employed in the generation of surface roughness in curing polymer
 157 melts (Marthelot *et al.* 2018; Jambon-Puillet *et al.* 2021), where centrifugal instabilities
 158 (Rietz *et al.* 2017) are harnessed to facilitate the formation of periodic patterns.

159 In sealed tubes, the effect of centrifugation on the shape of capillary interfaces has been
 160 exploited in spinning drop experiments (Vonnegut 1942; Rosenthal 1962; Princen *et al.*
 161 1967; Torza 1975). These experiments can measure very low interfacial tensions (Drellich
 162 *et al.* 2002), by rotating a horizontal tube containing a drop of lower-density liquid within a
 163 higher-density fluid. For high enough rotation rate, the (transverse) gravity acceleration can
 164 be neglected, and the equilibrium shape of the drop results from the balance of the centrifugal

165 force, that tends to elongate the drop along its axis (and thus to thicken the surrounding liquid
166 film), with surface tension, that promotes a spherical shape.

167 In this context, Manning *et al.* (2011) studied the case of a tube of inner radius R partially
168 filled with a liquid of density ρ and surface tension γ , rotated around its symmetry axis at
169 angular velocity ω under weightlessness. They derived a criterion for the occlusion of the
170 tube by a static meniscus spanning the cross-section of the channel, with a contact angle ϕ ,
171 and computed a critical angular velocity ω_0 :

$$172 \quad \frac{\rho\omega_0^2 R^3}{\gamma} = 32 \sin^3 \left(\frac{\pi + 2\phi}{6} \right), \quad (2.1)$$

173 such that the tube cannot occlude if $\omega > \omega_0$. In the case of an occluding meniscus forming
174 a bubble, the gas-liquid interface meets the solid wall tangentially, i.e. $\phi = 0$. Thus, Eq.(2.1)
175 indicates that under weightlessness, the bubble cannot occlude the channel if $\rho\omega^2 R^3/\gamma > 4$.

176 To the best of our knowledge though, the combined effect of axial gravity and transverse
177 centrifugal force on the rising motion of long bubbles in a vertical setting has not been
178 studied yet. Building on the demonstrated ability of centrifugation to elongate light drops
179 or bubbles in tubes, and thereby to thicken their lubricating film, we now study how
180 centrifugation can facilitate the release of long bubbles that are trapped in sealed capillaries
181 due to surface tension.

182 We consider a long bubble of length L immersed in a viscous fluid of dynamic viscosity
183 μ , density ρ , and surface tension γ , both contained in a vertically-oriented circular tube of
184 radius $R \ll L$, sealed at both ends. The bubble ascends along the vertical axis at a constant
185 velocity U_b under the influence of gravity. The tube's radius is assumed to be of the order
186 of the capillary length $\ell_c = \sqrt{\gamma/\rho g}$, where g is the acceleration due to gravity, so that the
187 Reynolds number $Re = \rho U_b R / \mu$ is sufficiently small to neglect any inertial effects.

188 Bretherton's solution describing the bubble's ascent at a constant velocity is valid only
189 if the tube radius exceeds a critical value $R_c \approx 0.918\ell_c$. As the tube radius R approaches
190 this critical value, the bubble's ascending speed diminishes, eventually reaching zero. This
191 phenomenon can be explained through a simple mass conservation consideration: the sealed
192 tube requires the rising bubble to displace the liquid above, creating drainage through its
193 peripheral lubricating film. However, for $R < R_c = 0.918\ell_c$, surface tension becomes
194 dominant, causing the bubble to expand and occupy the entire tube cross-section, preventing
195 liquid drainage.

196 We now examine the scenario where the vertical tube undergoes constant rotation around
197 its symmetry axis with an angular velocity ω . We can readily anticipate that the centrifugal
198 force will push liquid towards the solid tube wall, thickening the fluid film around the bubble
199 and facilitating its ascent. Therefore, a steady rising motion of the bubble may be achievable
200 even in tubes with $R < R_c$, provided the angular velocity ω is sufficiently high. In the
201 subsequent section, we revisit Bretherton's theory (Bretherton 1961) to predict the new
202 threshold $R_c(\omega)$ and the steady rising velocity U_b as a function of the rotational speed.

204 2.1. Theoretical prediction for the threshold and rising velocity

205 Since our focus lies in describing motion near the threshold characterized by a vanishing
206 velocity U_b , we preliminary assume a small capillary number $Ca = \mu U_b / \gamma \ll 1$. Viscous
207 stresses at the gas-liquid interface thus play a significant role only in regions where the fluid
208 is strongly confined, i.e. where the interface is very close to the solid wall. Consequently, the
209 upper part of the bubble's profile can be divided into two regions, see Figure 1(a). The outer
210 region corresponds to the top of the bubble (cap) where viscous effects are negligible : the

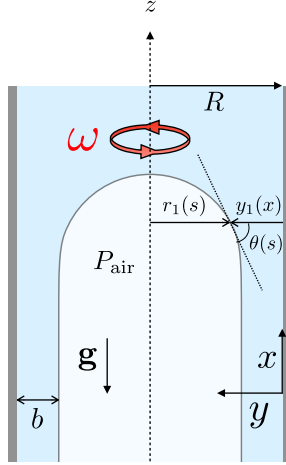


Figure 2: Sketch of the bubble in a vertical tube that rotates around its central axis with angular velocity ω . s is the arc-length of the interface measured from the tip of the bubble at $r = 0$. In the static cap region, the air-liquid interface is located by the distance $r_1(s)$ to the central axis, and the angle its tangent makes with the horizontal axis is denoted as $\theta(s)$. In the inner region, where a two-dimensional Cartesian system (x, y) is used, the interface is located instead by its distance from the solid wall $y_1(x)$.

equilibrium is controlled by an interplay between surface tension, gravity, and centrifugal forces. Conversely, a thin liquid film resulting from a balance between viscous, surface tension, gravity, and centrifugal forces defines an inner region of small axial curvature. We now derive the bubble's profiles in these two regions.

215 *The static cap*

216 In the outer region, the fluid around the cap of the bubble can be considered at rest (Bretherton
217 1961; Lamstae & Eggers 2017) so that in the cylindrical reference frame co-rotating with
218 the tube and translating with the bubble, the pressure P in the surrounding fluid satisfies:

$$219 \quad \mathbf{0} = -\nabla P + \rho\omega^2 r \mathbf{e}_r - \rho g \mathbf{e}_z. \quad (2.2)$$

220 By integrating the radial component of Eq. (2.2), we obtain

$$221 \quad P(r, z) = \frac{1}{2}\rho\omega^2 \left(r^2 - r_1(z)^2 \right) + \gamma\kappa + P_{\text{air}}, \quad \kappa = -\frac{1}{r_1(z) (1 + r'_1(z)^2)^{1/2}} + \frac{r''_1(z)}{(1 + r'_1(z)^2)^{3/2}} \quad (2.3)$$

222 where $r_1(z)$ and κ denote the location of the air-liquid interface measured from the central
223 axis (oriented upwards) and its curvature, respectively.

224 From the axial component of the momentum conservation equation Eq.(2.2), it follows
225 that:

$$226 \quad \gamma\kappa - \frac{1}{2}\rho\omega^2 r_1(z)^2 + \rho g z = \text{cst}. \quad (2.4)$$

227 By denoting as s the arclength of the interface profile measured from the tip of the bubble
228 and θ its tangent angle with respect to the horizontal (see Fig. 2), the static interface profile
229 is given by:

$$230 \quad -\gamma \left[\frac{d\theta}{ds} + \frac{\sin \theta}{r_1(s)} \right] - \frac{1}{2}\rho\omega^2 r_1(s)^2 + \rho g z(s) = \text{cst}, \quad (2.5)$$

231 where the coordinates $(r_1(s), z(s))$ locate the position of the gas-liquid interface at s in the
 232 (r, z) plane. Using that $\frac{dr_1}{ds} = \cos(\theta)$ and $\frac{dz}{ds} = -\sin(\theta)$, differentiating with respect to the
 233 curvilinear coordinate s gives:

$$234 \quad \gamma \left[\frac{d^2\theta}{ds^2} + \frac{\cos \theta}{r_1(s)} \frac{d\theta}{ds} - \frac{\cos \theta \sin \theta}{r_1(s)^2} \right] = -\rho \omega^2 r_1(s) \cos \theta - \rho g \sin \theta. \quad (2.6)$$

235 Finally, with the dimensionless variables $\bar{r}_1 = r_1/R$ and $\bar{s} = s/R$, Eq. (2.6) becomes:

$$236 \quad \frac{d^2\theta}{d\bar{s}^2} + \frac{\cos(\theta)}{\bar{r}_1} \frac{d\theta}{d\bar{s}} - \frac{\cos(\theta) \sin(\theta)}{\bar{r}_1^2} = -Bo \sin(\theta) - \bar{r}_1 Ce \cos(\theta), \quad (2.7)$$

237 where the Bond number $Bo = \frac{\rho g R^2}{\gamma} = (R/\ell_c)^2$ is introduced as the square of the ratio
 238 between the tube radius and the capillary length. The centrifugal number $Ce = \frac{\rho \omega^2 R^3}{\gamma}$ can be
 239 seen as a rotational Bond number where the centrifugal acceleration $R\omega^2$ plays the role of
 240 the gravitational acceleration.

241 For a given set of parameters (Bo, Ce) , two boundary conditions are required to integrate
 242 Eq.(2.7) from the position $(r_1(s=0) = 0, z(s=0) = 0)$. A first condition is provided by
 243 the symmetry of the problem, that imposes $\theta(0) = 0$ at the top of the static cap. The second
 244 boundary condition will be determined upon matching of this static profile with the inner
 245 region's one.

246 *The thin film region*

247 In the inner region where the bubble is surrounded by a thin lubricating film, the film's
 248 thickness is extremely small compared to the tube's radius. Following Bretherton (1961),
 249 we thus neglect the azimuthal curvature of the air-liquid interface and consider the thin film
 250 region as planar instead of annular.

251 Under these assumptions, we introduce the two-dimensional, stationary, Cartesian coordi-
 252 nate system (x, y) , where $x = z - U_b t$ opposes gravity, and $y = R - r$ represents the distance
 253 to the solid wall. In the framework of the lubrication approximation, the viscous flow in
 254 the thin film is driven by a pressure gradient resulting from a combination between gravity,
 255 capillarity and centrifugal force. The axial velocity accordingly writes (See Appendix A.1
 256 for a detailed derivation):

$$257 \quad u(x, y) = \frac{\gamma}{2\mu} \left(-y_1''' + \frac{\rho \omega^2 R}{\gamma} y_1' + \frac{\rho g}{\gamma} \right) (y^2 - 2y_1 y) - U_b, \quad (2.8)$$

258 where $y_1(x)$ denotes the distance of the air-liquid interface to the solid wall of the tube,
 259 and the prime denotes the derivative with respect to x . In Eq. (2.8), the first term of the
 260 right-hand-side stems from surface tension effects, the second from the centrifugal force and
 261 the third from gravity. Upon integration within the thin film, the volume flux reads:

$$262 \quad Q = -2\pi R U_b y_1 - 2\pi R \frac{\gamma}{3\mu} \left(-y_1''' + \frac{\rho \omega^2 R}{\gamma} y_1' + \frac{\rho g}{\gamma} \right) y_1^3. \quad (2.9)$$

263 This flux must equate the volume of fluid displaced per unit time by the top of the bubble,
 264 that is equal to $\pi R^2 U_b$. Since $y_1/R \ll 1$, the $-2\pi R U_b y_1$ term in the expression of the flow
 265 rate is a negligible correction. Finally, by imposing flux continuity with the region far away
 266 from the tip, where the film thickness can be considered as uniform and equal to a constant
 267 b , we obtain the following thin film equation:

268

$$y_1''' = \frac{\rho g}{\gamma} \left(1 - \frac{b^3}{y_1^3} \right) + \frac{\rho \omega^2 R}{\gamma} y_1'. \quad (2.10)$$

269 Since b is the length scale governing the flow in the inner region, we nondimensionalize, as
270 in Bretherton (1961), with:

271

$$y_1 = \eta b, \quad x = \zeta b (\rho g b^2 / \gamma)^{-1/3}, \quad (2.11)$$

272 This leads to the ordinary differential equation:

273

$$\eta''' = \frac{\eta^3 - 1}{\eta^3} + a\eta'. \quad (2.12)$$

274 where $a = \frac{C_e}{Bo^{2/3}} \left(\frac{b}{R} \right)^{2/3}$. In Eq. (2.12), the left-hand side represents the surface tension
275 term, while on the right-hand side, the first term accounts for gravity, the second for viscous
276 dissipation, and the third for the effect of centrifugation.

277 *Matching*

278 We aim at matching the inner solution, that is described by Eq.(2.12), with the static cap
279 solution provided by Eq.(2.6). Given that $b \ll R$, this requires taking the limit $\eta \rightarrow \infty$ in Eq.
280 (2.12) for the inner solution. In this limit, the equation behaves as:

281

$$\eta''' = 1 + a\eta', \quad (2.13)$$

282 whose general solution reads :

283

$$\eta = c_1 e^{\sqrt{a}\zeta} + c_2 e^{-\sqrt{a}\zeta} + c_3 - \frac{\zeta}{a}. \quad (2.14)$$

284 The values of c_1 , c_2 , and c_3 can be found through interpolation using the numerical solution
285 of the complete equation Eq.(2.12), whose initial conditions are obtained from the uniform
286 film solution. Indeed, when $\eta \rightarrow 1$, Eq. (2.12) becomes

287

$$\eta''' = 3(\eta - 1) + a\eta', \quad (2.15)$$

288 for which the only non-oscillating solution is: $\eta_0 = 1 + C \exp(\mathcal{F}\zeta)$, where C is an integration
289 constant and:

290

$$\mathcal{F} = \frac{\left(\frac{2}{3} \right)^{1/3} a}{\left(27 + \sqrt{3} \sqrt{243 - 4a^3} \right)^{1/3}} + \frac{\left(27 + \sqrt{3} \sqrt{243 - 4a^3} \right)^{1/3}}{2^{1/3} 3^{2/3}}. \quad (2.16)$$

291 Since the value of C can be adjusted by shifting the origin of ζ , we can set $C = 1$ and
292 a large, negative initial value ζ_0 to initialize the integration. This procedure yields initial
293 conditions for the full non-linear equation Eq.(2.12), i.e.:

294

$$\eta(\zeta_0) = 1 + \exp(\mathcal{F}\zeta_0), \quad \eta'(\zeta_0) = \mathcal{F} \exp(\mathcal{F}\zeta_0), \quad \eta''(\zeta_0) = \mathcal{F}^2 \exp(\mathcal{F}\zeta_0).$$

295 We solve Eq.(2.12)[†] to obtain the inner solution η for various values of a , and fit the outer
296 profile $\eta = c_1 e^{\sqrt{a}\zeta} + c_2 e^{-\sqrt{a}\zeta} + c_3 - \frac{\zeta}{a}$ in the region where $\eta \gg 1$. This allows us to retrieve
297 the coefficients $c_1(a)$, $c_2(a)$ and $c_3(a)$. From Figure 3(a), it is evident that the outer profile η

[†] Using the built-in MATLAB ODE solver *ode45*.

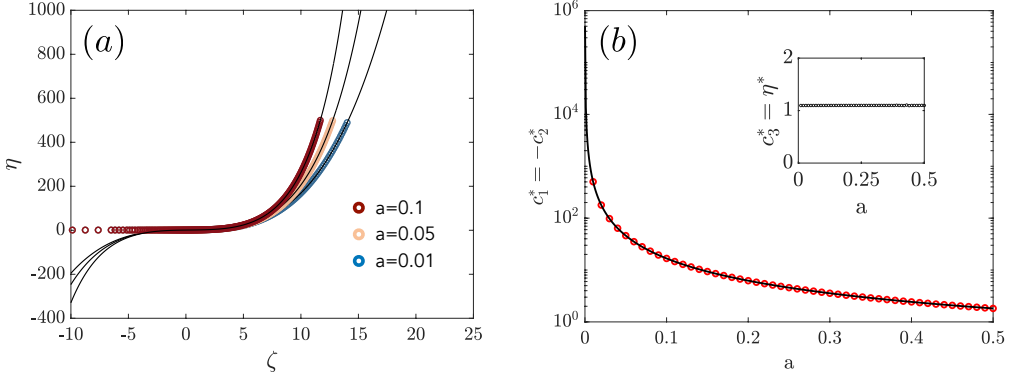


Figure 3: (a) The inner region profile η as a function of the dimensionless height ζ . The dots represent the solution η of the full equation Eq.(2.12) for various values of a , while the black solid lines represent the outer profile of the inner region

$\eta = c_1 e^{\sqrt{a}\zeta} + c_2 e^{-\sqrt{a}\zeta} + c_3 - \frac{\zeta}{a}$, where $c_1(a)$, $c_2(a)$ and $c_3(a)$ are obtained by fitting with the full inner solution, in the $\eta \gg 1$ region. The outer profiles clearly exhibit an inflection point, at a distance referred to as $\zeta^*(a)$. For each value of a , the origin is then shifted so that $\eta''(0) = 0$. (b) Shifted coefficient $c_1^* = -c_2^*$ as a function of a (red dots). The black solid line corresponds to $c_1^* = 0.500a^{-3/2} + 0.286a^{-1/2}$. (Inset) Shifted coefficient $c_3^* = \eta(0) \equiv \eta^*$ as a function of a . This coefficient does not vary significantly with a .

298 of the inner solution exhibits an inflection point. We thus translate the origin to the position
299 where $\eta'' = 0$, located at the coordinate:

$$300 \quad \zeta^* = \frac{1}{2\sqrt{a}} \log \left(-\frac{c_2}{c_1} \right). \quad (2.17)$$

301 Using the shifted variable $\chi = \zeta - \zeta^*$, we can now define $\eta(\chi) = c_1^* e^{\sqrt{a}\chi} + c_2^* e^{-\sqrt{a}\chi} + c_3^* - \frac{\chi}{a}$,
302 where the new coefficients c_1^* , c_2^* , and c_3^* are expressed as:

$$303 \quad c_1^* = c_1 e^{\sqrt{a}\zeta^*} = c_1 \sqrt{-\frac{c_2}{c_1}} = \text{sgn}(c_1) \sqrt{-c_1 c_2}, \quad (2.18a)$$

$$305 \quad c_2^* = c_2 e^{-\sqrt{a}\zeta^*} = c_2 \sqrt{-\frac{c_1}{c_2}} = \text{sgn}(c_2) \sqrt{-c_1 c_2}, \quad (2.18b)$$

$$307 \quad c_3^* = c_3 - \frac{\zeta^*}{a} = c_3 - \frac{1}{2a^{3/2}} \log \left(-\frac{c_2}{c_1} \right) = \eta(\chi = 0). \quad (2.18c)$$

308 The new coefficients are well fitted (see Figure 3(b)) by:

$$309 \quad c_1^* = -c_2^* \approx 0.500a^{-3/2} + 0.286a^{-1/2}, \quad (2.19a)$$

$$311 \quad c_3^* \approx 1.10, \text{ independently of the value of } a. \quad (2.19b)$$

312 Thus, the distance from the wall at which the outer profile exhibits an inflection point can
313 be evaluated as:

$$314 \quad y_1(0) = \eta(0)b = (c_1^* + c_2^* + c_3^*)b \approx 1.10b \ll R. \quad (2.20)$$

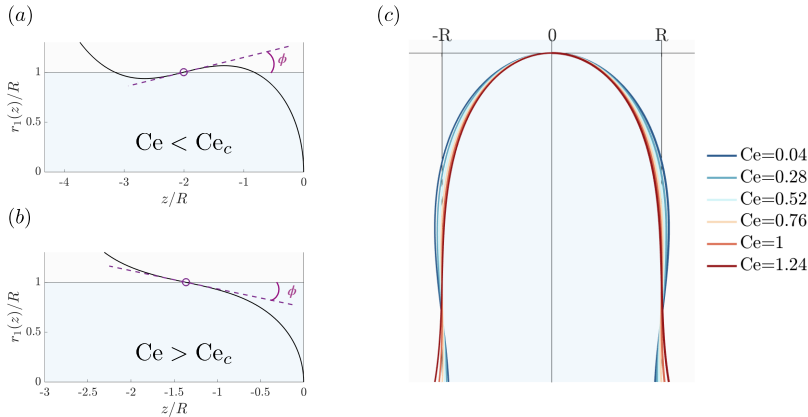


Figure 4: Static cap profile for a Bond number $Bo = 0.55$, and a centrifugal number Ce that is (a) below and (b) above the threshold $Ce_c(Bo)$. Below the threshold, the slope $r'_1(z)|_{r=R}$ is positive at the inflection point, causing the upper profile to escape the fluid domain $r < R$. ϕ is the angle between the tangent to the static cap profile at the wall and the vertical axis: $\phi = \tan^{-1}(-r'_1(z)|_{r=R})$ and is thus negative in case (a) and positive in case (b). (c) Evolution of the static cap profile at fixed $Bo = 0.55$, when increasing Ce from a value below the threshold $Ce_c \approx 1$ to a value slightly above threshold.

315 Furthermore, the slope of the profile at the inflection point is given by:

$$y'_1(0) = \eta'(0) \left(\rho g b^2 / \gamma \right)^{1/3} = \left(c_1^* \sqrt{a} - c_2^* \sqrt{a} - \frac{1}{a} \right) \left(\rho g b^2 / \gamma \right)^{1/3} = 0.572 \left(\rho g b^2 / \gamma \right)^{1/3} > 0. \quad (2.21)$$

316 Remarkably, the conditions on film thickness Eq.(2.20) and slope Eq.(2.21) at the inflection
317 point are the same as described in Bretherton (1961). Therefore, the centrifugal force alters
318 the inner region solution and the static cap profile, but the matching conditions (and thus the
319 boundary conditions for the static cap solution) remain surprisingly unchanged from those
320 of Bretherton (1961).

321 The above analysis provides the missing information required to solve the static cap profile
322 described by Eq. (2.7). Specifically, the static profile for a given set of parameters (Bo, Ce)
323 is obtained through a shooting method, searching for the first derivative $\dot{\theta}_0$ at the tip of the
324 cap, that is such that the integration of Eq.(2.7) from initial conditions $(\theta_0 = 0, \dot{\theta}_0)$ results
325 in a profile where the inflection point $\ddot{r}_1(z) = 0$ is reached for $r_1(z) = R$. The numerical
326 integration of Eq.(2.7) is performed using the MATLAB built-in ODE solver `ode23t`, with a
327 spacing along the curvilinear coordinate of $0.01R$, while the shooting method is implemented
328 by means of the non-linear MATLAB system solver `fsover`. The resulting slope $r'_1(z)|_{r=R}$ at
329 the inflection point is then computed from the generated profile.

330 For fixed $Bo < Bo_{c,0} = (R_c/\ell_c)^2$ and varying Ce numbers, it appears that some profiles
331 are unphysical: below a critical value Ce_c that depends on the Bond number Bo , the static cap
332 shape exhibits a positive slope at the inflection point at the solid wall, causing the upper profile
333 to extend beyond the fluid domain $r < R$, as illustrated in Figure 4, which is not compatible
334 with the matching condition $0 < y'_1(0) = -r'_1(z)|_{r=R}$. By progressively increasing the
335 centrifugal number Ce , the slope at the inflection point at the wall decreases, leading to a
336 reduction of the bulge outside the fluid domain, as shown in Figure 4(c). Ultimately, for
337 $Ce > Ce_c$, the slope becomes negative, causing the entire static cap to reside within the fluid
338 domain, see Figure 4(b) and (c).

340 In the following, we denote as ϕ the resulting angle between the liquid-air interface and
 341 the vertical axis at the inflection point, i.e. $\phi = \tan^{-1}(-r'_1(z)|_{r=R}) = \tan^{-1}(y'_1(0))$. A closer
 342 inspection reveals that within a small range around Ce_c , i.e. for $|Ce - Ce_c(Bo)| < 0.2$, ϕ
 343 varies linearly with Ce , as shown in Figure 5(a). Within this range, the angle ϕ (in radians)
 344 is well approximated by:

$$345 \quad \phi(Ce, Bo) \approx 0.144(Ce - Ce_c(Bo)). \quad (2.22)$$

346 where the factor 0.144 is independent from Bo (up to variations less than 0.001 radians).
 347 Interestingly, this prediction is consistent with the occlusion criterion derived by Manning
 348 *et al.* (2011) under weightlessness (i.e. $Bo = 0$), reported in the introduction of this section
 349 (Eq.(2.1)). Indeed, ϕ represents the slope of the gas-liquid interface at the inflection point,
 350 located at a distance $1.10b$ from the solid wall of the tube (Eq.(2.20)). In this sense, it can be
 351 seen as the contact angle of a meniscus occluding a virtual channel of radius ($R - 1.10b$),
 352 rotating at angular velocity ω . Thus, in the absence of gravity, and in the limit of small
 353 contact angle ϕ , the occlusion criterion Eq.(2.1) becomes :

$$354 \quad Ce(\phi, Bo=0) = \frac{\rho\omega^2(R - 1.10b)^3}{\gamma} = 32 \sin^3\left(\frac{\pi + 2\phi}{6}\right) \approx 4\left(1 + \sqrt{3}\phi\right), \quad (2.23)$$

355 which can be recasted as $\phi(Ce, Bo = 0) \approx 0.144(Ce - Ce_{c,0})$, where $Ce_{c,0} \equiv Ce_c(Bo = 0) = 4$.

356 Thus, at fixed Bo , the critical centrifugal number $Ce_c(Bo)$ for vanishing angle ϕ (or
 357 equivalently for vanishing slope) is retrieved as the value of Ce at which the best linear fit
 358 of $\phi(Ce, Bo)$ cancels out. Its dependency on the Bond number is depicted in Figure 5(b).
 359 Note that we performed a convergence analysis and observed no further variations of Ce_c ,
 360 within a tolerance of 0.07%, when increasing 10 times the resolution on the spacing along the
 361 curvilinear coordinate used to integrate the static cap profiles. For $Ce < Ce_c$, the geometrical
 362 constraint $\phi = \tan^{-1}(y_1(0)) \approx y'_1(0) > 0$ cannot be satisfied, so that this value corresponds
 363 to the threshold for the onset of motion.

364 A second-order polynomial approximation of $(Ce_c(Bo), Bo)$ is: $Bo \approx 0.842 -$
 365 $0.295 Ce_c(Bo) + 0.020 Ce_c^2(Bo)$, whose solution, shown in Figure 5(b), reads:

$$367 \quad Ce_c = \frac{0.295 - \sqrt{0.295^2 - 0.080(Bo_{c,0} - Bo)}}{0.040}, \quad (2.24)$$

368 where $Bo_{c,0} = 0.842$ is the critical Bond number in the absence of centrifugation ($Ce = 0$).
 369 Note that in the limit $Bo \rightarrow 0$, the approximation Eq.(2.24) yields $Ce_c(Bo = 0) \approx 3.9$, that
 370 is close to the threshold $Ce_{c,0} = 4$ computed by Manning *et al.* (2011) under weightlessness.
 371 Conversely, in the limit ($Ce_c \rightarrow 0$, $Bo \rightarrow Bo_{c,0}$), Eq.(2.24) simplifies into:

$$372 \quad Ce_c \approx \frac{1}{0.295}(Bo_{c,0} - Bo). \quad (2.25)$$

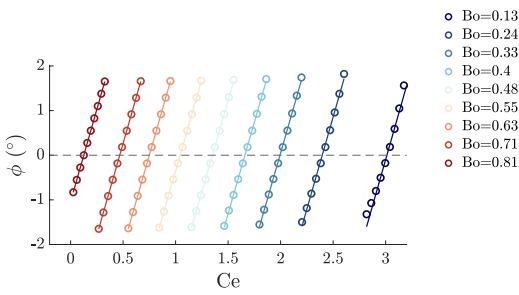
373 By injecting Eq. (2.25) into Eq. (2.22), we obtain, in the limit $Ce \rightarrow 0$:

$$374 \quad \phi \approx 0.49(Bo - (Bo_{c,0} - 0.295Ce)), \quad (2.26)$$

375 reminiscent of the expression derived by Bretherton for a non-rotating capillary tube
 376 ($\phi = 0.49(Bo - Bo_{c,0})$). The similarity of these expressions highlights the role of the
 377 centrifugation as a downward shift in the critical Bond number for the onset of motion.

378
 379 In addition, this analysis provides a prediction for the rising velocity of the bubble for
 380 $Ce > Ce_c(Bo)$. Indeed, for Ce close enough to the threshold $Ce_c(Bo)$, the slope of the inner

(a)



(b)

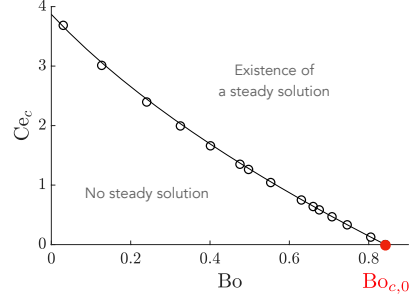


Figure 5: (a) Angle ϕ of the static cap profile between the vertical axis and the tangent to the static cap profile (obtained by integrating Eq. (2.7) while requiring that the interface reaches the solid wall with an inflection point), as a function of the centrifugal number C_e , for various Bond numbers Bo . The dots are the values computed from the shape of the interface, while the solid lines are the best linear fit. For each Bo , the critical centrifugal number C_{e_c} is defined as the value of C_e for which the best linear fit cancels out. (b) The critical centrifugal number C_{e_c} as a function of the Bond number Bo . At a given value of Bo , the matching with the inner region is only possible if $C_e > C_{e_c}(Bo)$. The dots are the values of C_e that cancel the linear approximation of $\phi(C_e, Bo)$ for each Bond number, while the dotted back line represents the approximation Eq.(2.24). The red dot with coordinates $(Bo_{c,0} = 0.842, C_{e_c} = 0)$ locates the threshold in the absence of centrifugation.

381 solution at the inflection point should verify, using Eq.(2.20), (2.21), and (2.22):

$$y'_1(0) = 0.572 \left(\rho g b^2 / \gamma \right)^{1/3} = \tan(\phi) \approx \phi \approx 0.144 \left(\frac{\rho \omega^2 (R - 1.10.b)^3}{\gamma} - C_{e_c}(Bo) \right). \quad (2.27)$$

382

383 Since the volume of fluid displaced per unit time by the tip of the bubble $\pi R^2 U_b$ should be
384 equal to the volume flux in the uniform film region, we can relate the thickness b to the
385 inner radius R and the velocity U_b through $\rho g b^3 / 3\mu U_b = R/2$. Expanding Eq.(2.27) up to
386 first order in (b/R) yields the following expression of Ca as an implicit function of C_e and
387 Bo :

$$388 \quad C_e - C_{e_c} = 3.78 C_e \left(\frac{Ca}{Bo} \right)^{1/3} + 4.35 Bo^{1/3} \left(\frac{Ca}{Bo} \right)^{2/9}, \quad (2.28)$$

389 where C_{e_c} is the function of Bo described above. The ratio Ca/Bo compares the bubble
390 velocity U_b to the settling velocity $U^* = \rho g R^2 / \mu$. Note that Eq.(2.28) admits an analytical
391 solution: by setting the unknown $x = (Ca/Bo)^{1/9}$, Eq.(2.28) can indeed be recasted as an
392 equation of the type $x^3 + a_1 x^2 + a_2 x + a_3 = 0$.

393 2.2. Experiments on centrifugated bubbles

394 In this section, we outline our experimental setup and procedure and compare the results
395 against the above theoretical developments.

396 Experimental setup and procedure

397 Cylindrical borosilicate capillary tubes (Hilgenberg GmbH) are partially filled with silicone
398 oil (Sigma Aldrich, $\rho = 964 \text{ kg/m}^3$, $\mu = 9.64 \times 10^{-2} \text{ Pa.s}$, $\gamma = 2.09 \times 10^{-2}$), leaving an air
399 bubble with a length L greater than 10 times the radius R of the tube. Both ends of the tubes
400 are sealed with epoxy resin. The inner radii of the tubes used in our experimental campaign

401 vary between 0.8 mm and 1.3 mm, corresponding to Bond numbers $Bo \equiv \rho g R^2 / \gamma$ in the
 402 range [0.29, 0.76]. Note that the uncertainty in the inner diameters of the tubes is of 0.05
 403 mm.

404 The tube attachment system, presented in Figure 6(a), consists of two circular mounts made
 405 of PETG, rigidly connected together via two vertical steel rods, and linked by bearings to a
 406 fixed aluminium frame (not represented in the Figure). On each mount, a central, threaded
 407 circular mouthpiece accommodates a hollow cylinder whose inner radius matches the outer
 408 radius of the capillary tube. The extremities of the tube are then inserted into these cylinders,
 409 and securely clamped to the mounts using a clamping chunk. By this means, the tube can
 410 be easily replaced by a capillary of a different size with minimal adjustments of the setup.
 411 The lower mount is also connected to the shaft of a DC motor that imposes the rotation of
 412 the tube attachment system. While the tube, the mounts and the rods rotate collectively, the
 413 verticality and stability of the whole setup are ensured by the fixed aluminium frame.

414 The motor is voltage-controlled to achieve the desired rotation speed, measured with less
 415 than 1% error using a tachometer. To enhance visualization, a LED panel is positioned behind
 416 the tube attachment system.

417 A Basler camera records the evolution of the bubble in the tube, and the velocities of the
 418 upper and lower caps of the bubble are obtained through image post-processing performed
 419 via a custom MATLAB script. Specifically, a column of pixel aligned with the tube that crosses
 420 the upper and bottom profiles of the bubble, is extracted from each frame. These slices are
 421 then juxtaposed to each other into an image where the horizontal axis represents time. The
 422 displacement of the bubble extremities with time are clearly visible on the resulting image,
 423 as shown in Figure 6(c).

424 Once the motor is switched on, a transient regime occurs where the upper cap of the bubble
 425 rises while the bottom cap remains immobile, resulting in the bubble elongation, reminiscent
 426 of spinning bubbles experiments (Vonnegut 1942). This is accompanied by the progressive
 427 thickening of the surrounding film that propagates from the top to the lower cap of the bubble,
 428 as seen in Figure 6(b). Once the propagation front reaches the bottom extremity, the lower
 429 cap starts its ascent at the same (constant) velocity as the upper cap, see Figure 6(c). The
 430 rising regime is assumed to be stationary if the difference between the caps' velocities is less
 431 than 5%. The bubble velocity is computed as the mean velocity between the upper and the
 432 bottom cap velocities.

433 For a given inner radius R and a fixed rotational speed ω , both Bo and Ce are fixed. The
 434 capillary number $Ca = \mu U_b / \gamma$ is then derived from the measurement of the bubble velocity
 435 at steady state U_b . For the experiments reported in this Section, we specify that the Bond
 436 number remains smaller than the threshold $Bo_c = 0.842$. Thus, the bubble does not move at
 437 all if the rotational speed is zero. To avoid excessively long working time for the motor, we
 438 did not operate it more than 8 hours consecutively. Considering that with our experimental
 439 setup, we cannot precisely detect a motion smaller than 1 mm between the start and the
 440 end of an experiment, the smallest capillary number that is experimentally measurable is
 441 $Ca_{\min} = 1.6 \times 10^{-7}$. A value inferior to this limit will be accordingly set equal to zero. The
 442 maximal rotational speed achieved by the DC motor is $\omega_{\max} = 400 \text{ rad.s}^{-1}$. For a given tube
 443 inner radius, this sets a limit on the maximal centrifugal number Ce_{\max} that is experimentally
 444 reachable.

445 *Experimental results and comparison with the theoretical threshold*

446 For comparison with the theoretical threshold for the onset of motion, we present our
 447 experimental findings in the (Bo, Ce) diagram featured in Figure 7(a). Overall, the theoretical
 448 prediction is quantitatively consistent with the experimental results, that reveal a rapid decay
 449 in the bubble velocity as the centrifugal number Ce approaches the theoretical threshold

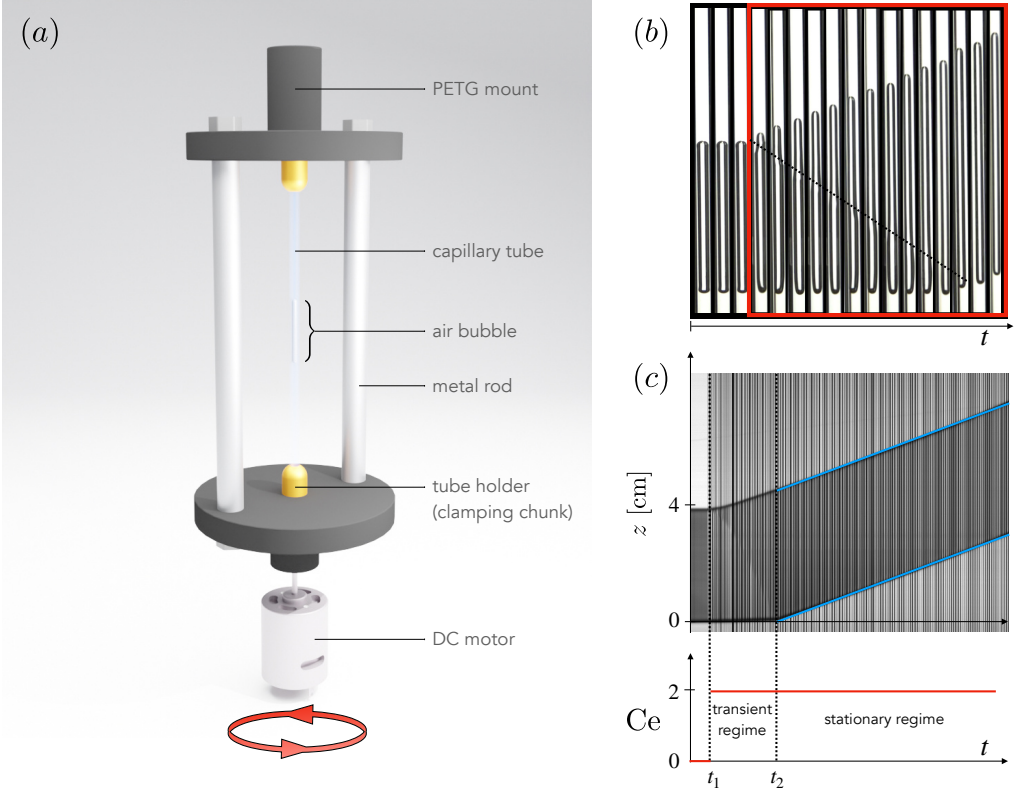


Figure 6: Experimental setup and post-processing for rotating bubbles. (a) Tube attachment system. The capillary tube is clamped on both extremities to mounts connected together by two metal rods. The bottom mount is linked to the shaft of a DC voltage-controlled motor that imposes the rotation of the system around its central, vertical axis. (b) Photographs of a long bubble inside a tube filled with silicone oil, at different and equally spaced time steps within the transient regime. In the red frame, the motor has been switched on and the upper cap starts rising while the bottom cap remains still. Along with the resulting bubble elongation, the surrounding liquid film gets progressively thicker from the top to the bottom part of the bubble. The dotted line roughly locates the position of the propagation front. Once the front has reached the lower cap, it starts rising. (c) Intensity profile as a function of time along the tube axis. To produce this image, a column of pixel aligned with the central axis of the tube is extracted from each frame of the movie. The columns are then juxtaposed to each other. The locations of the upper and lower cap as a function of time are easily identified as the two roughly parallel black curves limiting a darker domain that corresponds to the position of the bubble itself. At time t_1 , the motor is switched on. At t_2 , the bubble dynamics reaches a stationary state: the upper and lower caps rise at same constant velocity, as highlighted by the parallel blue solid lines that are superimposed on the position of the caps as a function of time. For (b) and (c), $R = 1.2\text{mm}$ and $\text{Ce} = 1.97$. The transient duration is approximately equal to $t_2 - t_1 \approx 130\text{s}$ and the capillary number computed from the steady state is $\text{Ca} \approx 3.03 \times 10^{-4}$.

450 $\text{Ce}_c(\text{Bo})$. As it was challenging to precisely determine the experimental threshold, we
 451 endeavored to establish a narrow range by identifying the highest $\text{Ce} \equiv \text{Ce}_{c,\text{exp}}$ for which the
 452 bubble displacement fell below our detection limit. This lower bound is denoted by red crosses
 453 on Figure 7(a), and closely align with the theoretical threshold. However, the prediction is
 454 less precise for the smallest values of Bo : the experimental threshold is downward-shifted
 455 with respect to the theoretical prediction.

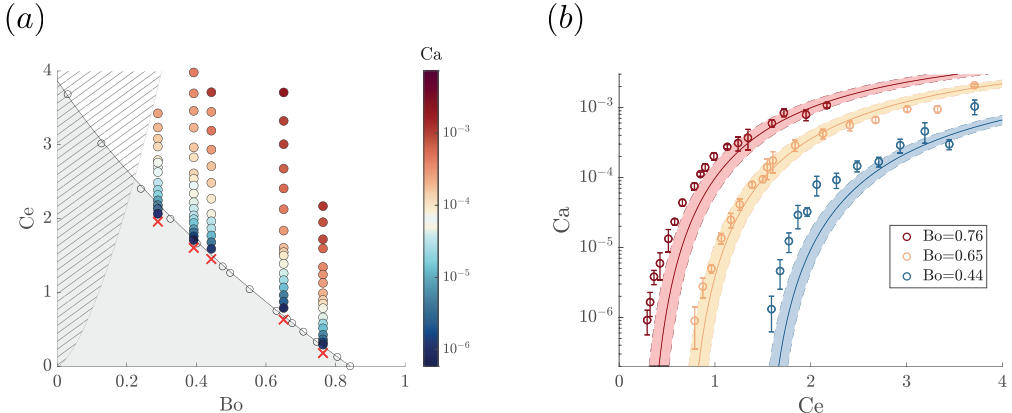


Figure 7: (a) Diagram (Bo , Ce), where each dot corresponds to a measurement of $Ca > 0$ for a given set of parameters (Bo, Ce) . The red crosses indicate the couples $(Bo, Ce = Ce_{c,\exp}(Bo))$ for which the bubble displacement fell below our detection limit. The black circles indicate the theoretical threshold for the onset of motion and the black solid line represents the approximation Eq.(2.24) of $Ce_c(Bo)$. Below this line, the gray area indicates the region of parameters where the steady rising of a bubble is not possible according to our theoretical analysis. Finally, the shaded area corresponds to the region of parameters that is not accessible with our setup, due to the constraints on the maximal angular velocity provided by the motor. (b) Capillary number Ca as a function of the centrifugal number Ce measured for various Bond numbers. The dots are the experimental points, and for each Bond number Bo , the solid line is the theoretical prediction Eq.(2.28), computed using the corresponding experimental value of Bo indicated in the legend. The dotted lines also represent the prediction Eq.(2.28), but for $Bo \pm \Delta Bo$, where ΔBo accounts for the ± 0.05 mm uncertainty on the tube inner diameters. The errorbars represent the measurement uncertainty on the bubble velocity.

456 Figure 7(b) reports measurements of the bubble velocity as a function of the rotational
457 speed. The trend is satisfactorily captured by Eq.(2.28). We note however that close to the
458 threshold, the measured velocities are in general higher than predicted, consistently with the
459 downward shift of the experimental threshold mentioned above. We believe that this can be
460 ascribed to horizontal vibrations of the tube attachment system observed while operating the
461 motor. As observed by Kubie (2000), the rising velocity of a Taylor bubble within a vertical
462 tube is indeed larger when the tube is oscillated in the horizontal plane, and increases with
463 the oscillation acceleration. This hypothesis is backed up with the photographs of rotating
464 bubbles along their ascent, that show some asymmetry of the bubble profile with respect to the
465 tube axis, as can be seen for instance in Figure 6(b). This is compatible with the observations
466 of Kubie (2000) under horizontal oscillations: the relative position of the bubble moves
467 periodically from one side of the tube to the other, which thickens the lubricating film on
468 one or the other side of the bubble, resulting in a more efficient drainage and thus in faster
469 bubble ascent.

470 Despite these discrepancies, our theoretical analysis seems to provide a good estimation
471 of the threshold for the onset of motion and a satisfying prediction for the general trend of
472 the rising velocity as a function of the rotational speed.
473

474 In summary, rotation reduces the critical tube radius for the onset of motion and facilitates
475 bubble ascent. From a theoretical point of view, the most appreciable effect of centrifugation
476 is the modification of the static cap profile, while geometrical constraints stemming from
477 the matching with the thin film region appear remarkably unchanged from the classical case

478 without rotation. At the same time, experiments demonstrate the thickening of the thin film
 479 surrounding the elongated part of the bubble, for increasing rotational speed. This thickening
 480 is caused by the centrifugal acceleration which induces a radial, "gyrostatic" pressure gradient
 481 that pushes liquid towards the solid wall. We can thus interpret centrifugation as a mean to
 482 tune the thickness, and thus the flow rate within the gap between the tube wall and the bubble,
 483 resulting in the lowering of the critical Bond number for the onset of motion.

484 An alternative and simple strategy to modify the hydrostatic pressure gradient is to tilt the
 485 tube with respect to gravity, whose effect is investigated in the next Section.

486 3. Effect of tilt

487 The influence of inclination angle on the mobility of elongated bubbles was first observed
 488 by White & Beardmore (1962), who pointed out the necessity of careful positioning of
 489 the pipes for precise measurement of the rising velocity. Since then, many studies have
 490 been dedicated to the motion of long bubbles in inclined pipes (Zukoski (1966), Maneri &
 491 Zuber (1974), Bendiksen (1984), Weber *et al.* (1986), Couët & Strumolo (1987), Shosho
 492 & Rya (2001), Boucher *et al.* (2023) among others). All studies reported a non-monotonic
 493 dependency of the rising velocity on the tilt angle: starting from a horizontal position,
 494 the velocity of elongated bubbles increases with the inclination of the pipe, reaching a
 495 maximum value. Subsequently, the velocity decreases until the vertical position is attained.
 496 These observations are reminiscent of the so-called Boycott effect (Boycott 1920; Acrivos
 497 & Herbolzheimer 1979) in the case of settling suspensions in sealed tubes, as seminally
 498 observed by Boycott (1920) with blood corpuscles sedimenting in serum, that demonstrated
 499 a several-fold increase in their sedimentation rate when the tube was inclined.

500 Most of these analyses are interested in the inertial regime, with large Bond numbers,
 501 and only scarce studies were dedicated to the regime close to the onset of motion, that is
 502 dominated by surface tension (low Bond number). Zukoski (1966) conducted an extensive
 503 series of experiments focusing on the velocity of elongated bubbles in tubes within a large
 504 range of Bond numbers, delving into the impact of liquid viscosity and surface tension
 505 on bubble velocity. For low Bond number ($Bo = 0.870$), elongated bubbles exhibited no
 506 detectable movement in horizontal or vertical positions but could rise in inclined tubes with
 507 angles ranging from 20° to 80° with the horizontal, with a maximum velocity reached about
 508 50° . This observation suggests that tilting the tube with respect to gravity may enable the
 509 motion of long bubbles that are stuck in a vertical configuration owing to surface tension.

510 In a similar context, Collicott & Manning (2014) studied the stability of a liquid mass in a
 511 tube above a capillary interface spanning the cross-section of the channel, for various contact
 512 angles and tube inclinations with respect to gravity. At fixed contact angle, they computed
 513 the critical Bond number as the threshold above which the SURFACE EVOLVER simulations
 514 do not converge to a solution of finite axial extent, thereby identifying the critical Bond
 515 number as a stability threshold for the capillary interface. Within this approach, the critical
 516 Bond number for a 0° - contact angle should correspond to the stability threshold of a long
 517 static bubble, expanding over the entire cross-section of the tube. However, difficulties of
 518 modelling perfectly wetting conditions prevented the authors to compute the critical Bond
 519 number as a function of inclination in this case.

520 To the best of our knowledge, there is currently no predictive analysis of the mobility
 521 enhancement of long bubbles due to tilted gravity in very narrow capillaries. In this study,
 522 we investigate how the direction of gravity affects the mobility of long bubbles in the low Bo
 523 regime, focusing on the angle-dependent threshold for the initiation of motion.

524 3.1. Theoretical prediction for the threshold and rising velocity

525 The three-dimensional static cap

526 We first introduce the equilibrium equation for the static three-dimensional shape of the upper
 527 cap of the bubble. We define a Cartesian coordinate system (x, y, z) where z is the direction
 528 aligned with the central axis of the tube. The gravity vector reads $\mathbf{g} = (g \cos(\alpha), 0, -g \sin(\alpha))$,
 529 where α is the tilt angle of the tube ($\alpha = 90^\circ$ corresponds to a vertical tube), see Figure 8(a).

530 The evaluation of the static interface profiles of the upper cap is based on the two-
 531 dimensional Young-Laplace equation, where length scales are nondimensionalized with the
 532 tube radius (Manning *et al.* 2011; Rascón & Aarts 2017):

$$533 \quad \nabla \cdot \left(\frac{\nabla \bar{h}}{\sqrt{1 + (\nabla \bar{h})^2}} \right) = \text{Bo} (\cos(\alpha) \bar{x} - \bar{h} \sin(\alpha)), \quad (3.1)$$

534 where $\bar{h}(\bar{x}, \bar{y})$ denotes the height of the static cap; the quantity on the left hand side is the
 535 curvature κ of the liquid-gas interface while the term on the right hand side corresponds to the
 536 hydrostatic contribution. Eq.(3.1) is complemented with the boundary condition at the solid
 537 wall: $\frac{\nabla h}{\sqrt{1+(\nabla h)^2}} \cdot \mathbf{n} = -\cos(\phi)$, where \mathbf{n} is the outwards-oriented vector normal to the tube,
 538 and the angle ϕ is defined similarly as in the first part of this study, as the angle between \mathbf{e}_z
 539 and the tangent at the wall to the intersection of the liquid-gas interface with the plane $(\mathbf{n}, \mathbf{e}_z)$.
 540 We thus require the interface to reach the solid wall with a specified slope, that is assumed to
 541 be the same for all directions \mathbf{n} , for consistency with the matching with the thin film profile,
 542 assumed in the following to be radially symmetric. Note that this differs from the first part
 543 of this study, where we imposed a vanishing radial curvature at the wall and computed the
 544 angle ϕ a posteriori. Here, the the slope at the wall is specified as a boundary condition, with
 545 no requirement on the curvature. We acknowledge that requiring the gas-liquid interface to
 546 reach the wall for all directions \mathbf{n} is somehow counterintuitive, given that for small tilt angles
 547 α (i.e. for a strongly inclined tube with respect to gravity), we expect the film surrounding
 548 the bubble to be thicker in the direction $x > 0$, and the liquid-gas interface to be relatively far
 549 from the solid wall in this region. However, we focus here on the vicinity of the threshold for
 550 the onset of motion, where surface tension is dominant and causes the bubble to expand in
 551 the entire fluid domain $\sqrt{x^2 + y^2} = r < R$ in all directions, as experimentally observed (see
 552 for instance Figure 11(d)). The derivation of Eq.(3.1) can be found in Appendix B.

553 The thin film region and matching

554 Here, we opt for a simplified description of the inner region, that will be assumed to be
 555 radially symmetric. Neglecting the azimuthal curvature allows us to describe the bottom thin
 556 film with a two-dimensional, stationary Cartesian reference frame $(\tilde{x} = z - U_b t, \tilde{y})$, where
 557 $\mathbf{e}_{\tilde{x}}$ is aligned with the tube central axis and points upwards (such that $\mathbf{e}_{\tilde{x}} \cdot \mathbf{g} = -g \sin(\alpha)$),
 558 and $\mathbf{e}_{\tilde{y}}$ is the inward vector normal to the inner solid wall, such that $\mathbf{e}_{\tilde{y}} \cdot \mathbf{g} = -g \cos(\alpha)$, see
 559 Figure 8(b).

560 Within the lubrication framework, the viscous flow in the thin film is driven by Laplace
 561 and hydrostatic pressure gradients. The axial velocity in the bottom thin film accordingly
 562 writes (see Appendix A.2 for a detailed derivation):

$$563 \quad u(\tilde{x}, \tilde{y}) = \frac{\gamma}{2\mu} \left[-y_1''' + \frac{\rho g \cos(\alpha)}{\gamma} y_1' + \frac{\rho g \sin(\alpha)}{\gamma} \right] (\tilde{y}^2 - 2y_1 \tilde{y}) - U_b, \quad (3.2)$$

564 where y_1 denotes the distance of the air-liquid interface to the solid wall of the tube. Upon
 565 integration within the thin film and neglecting azimuthal variations of curvature and film

566 thickness, the volume flux reads:

$$567 \quad Q \approx -2\pi R U_b y_1 - 2\pi R \frac{\gamma}{3\mu} \left(-y_1''' + \frac{\rho g \cos(\alpha)}{\gamma} y_1' + \frac{\rho g \sin(\alpha)}{\gamma} \right) y_1^3, \quad (3.3)$$

568 Owing to mass conservation, this flux must be equal to the volume of fluid displaced per unit
569 time by the top of the bubble, which is $\pi R^2 U_b$. Given that $y_1/R \ll 1$, the term $-2\pi R U_b y_1$ in
570 the flow rate expression is a negligible correction. Finally, by enforcing flux continuity with
571 the region far from the tip, where the film thickness is uniformly constant and equal to b , we
572 derive the following thin film equation:

$$573 \quad y_1''' = \frac{\rho g \sin(\alpha)}{\gamma} \left(1 - \frac{b^3}{y_1^3} \right) + \frac{\rho g \cos(\alpha)}{\gamma} y_1'. \quad (3.4)$$

574 We nondimensionalize with:

$$575 \quad y_1 = \eta b, \quad \tilde{x} = \zeta b (\rho g b^2 \sin(\alpha)/\gamma)^{-1/3},$$

576 which leads to the ordinary differential equation:

$$577 \quad \eta''' = \frac{\eta^3 - 1}{\eta^3} + a \eta', \quad (3.5)$$

578 where $a = \cos(\alpha) \sin(\alpha)^{-2/3} \text{Bo}^{1/3} \left(\frac{b}{R} \right)^{2/3}$.

579 Upon introduction of the parameter a , this equation is exactly the same as Eq.(2.12)
580 describing the inner region in a centrifugated tube, that has been solved in Section 2.1. Thus,
581 shifting the origin to the position where $\eta'' = 0$, the distance from the wall at which the inner
582 solution exhibits an inflection point is:

$$583 \quad y_1(0) = \eta(0)b = 1.10b \ll R, \quad (3.6)$$

584 and the slope of the inner region profile at the inflection point is given by:

$$585 \quad y_1'(0) = \eta(0) \left(\rho g b^2 \sin(\alpha)/\gamma \right)^{1/3} = 0.572 \text{Bo}^{1/3} \sin(\alpha)^{1/3} \left(\frac{b}{R} \right)^{2/3} > 0. \quad (3.7)$$

586 For the matching of the thin film region with a two-dimensional cap, we would need to
587 determine the value of (positive) angle ϕ which leads to zero curvature at the wall. For the
588 matching with the previously introduced three-dimensional shape of the static cap, we extend
589 this analysis by searching for the angle ϕ that gives rise to zero radial curvature in *at least*
590 *one point* of the matching boundary. Note that although we imposed as a boundary condition
591 a constant angle ϕ at the interface when reaching the wall, the height of the interface at the
592 wall, and so the curvature, vary along the azimuthal direction. Since the angle ϕ at the point
593 of vanishing curvature should be positive according to the matching condition Eq.(3.7), we
594 identify the critical Bond number as the Bo value for which $\phi = 0$, and the radial curvature at
595 the wall vanishes in at least one point. For smaller Bond numbers, the geometrical constraint
596 on the slope cannot be satisfied in at least one point of the domain.

597 Eq.(3.1) together with its boundary conditions, is implemented in the Finite-Elements
598 solver Comsol Multiphysics. We exploit fourth-order Lagrangian shape functions, solving
599 for the height h and the mean curvature κ in a grid composed of quadrangular elements,
600 with 10 boundary layers of 1.3 stretching factor to properly capture the curvature at the
601 boundary. For each tilt angle α , solutions are obtained for different values of the angle ϕ
602 and Bond number Bo using the built-in Newton algorithm, initialized with the zero solution.
603 We then perform a continuation study by gradually decreasing the angle ϕ from 90° . Note

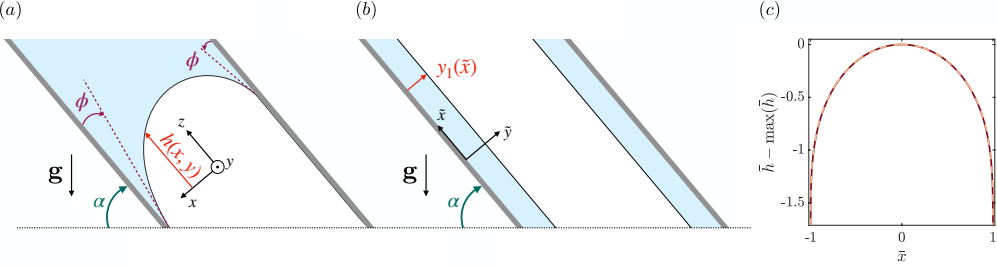


Figure 8: (a) Sketch of the static cap in a tube tilted with angle α with respect to the horizontal plane. A Cartesian coordinate system (x, y, z) is used, where z is the direction aligned with the central axis of the tube. The height of the liquid-air interface is denoted as $h(x, y)$ and the gas-liquid interface meets the wall with an angle ϕ , in all radial directions. (b) Sketch of the thin film region, assumed to be axisymmetric. A two-dimensional Cartesian coordinate system (\tilde{x}, \tilde{y}) is used, where \tilde{x} is the direction aligned with the central axis of the tube. The distance of the liquid-air interface from the solid wall is denoted by $y_1(\tilde{x})$. (c) Comparison between the solution of Eq.(3.1) (red solid line) and the axisymmetric solution of Eq.(2.6) with no rotation ($\omega = 0$) (pink dotted line), for tilt angle $\alpha = 90^\circ$ (vertical tube), $\phi = 0.50^\circ$ and Bond number $Bo = 0.86$.

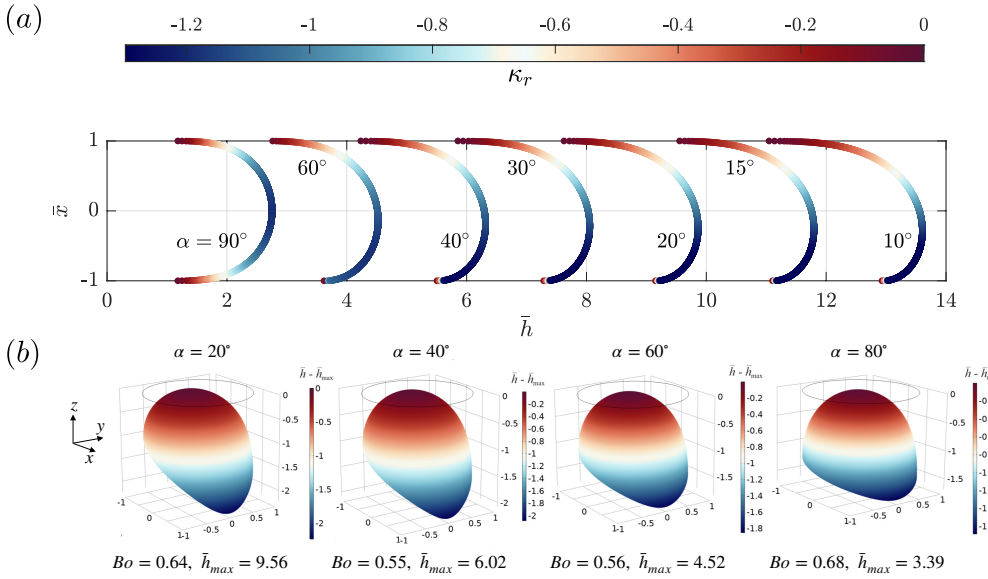


Figure 9: (a) Static cap profiles computed as solutions of Eq.(3.1) for various tilt angles α , with $\phi = 0.5^\circ$ and $Bo \gtrsim Bo_c(\alpha)$. The colorbar represents the radial curvature κ_r computed along the height profiles in the plane $y = 0$. The heights of the profiles for various α have been translated for visualisation purposes. (b) Three-dimensional static cap shape close to critical conditions $\phi = 0.5^\circ$, for various tilt angles. The colorbar represents the profile height $\bar{h} - \bar{h}_{\max}$.

that the boundary condition $\phi = 0^\circ$ cannot be imposed in this framework, as it implies infinite directional derivatives for the thickness. We thus study solutions in the close vicinity of $\phi = 0^\circ$ and extrapolate the retrieved behavior for $\phi \rightarrow 0$; however, this limitation will not significantly affect the evaluation of the threshold for the bubble rise. For fixed Bond number, a convergence analysis from a characteristic size of $0.05R$ to $0.01R$ (i.e. from 3200 to 33012 elements) showed variations of $\sim 10^{-4}$ rad in the value of ϕ resulting in a zero radial

610 curvature. The numerical code for $\alpha = 90^\circ$ (i.e. for a vertical tube), $\phi = 0.5^\circ$ and $Bo = 0.86$,
 611 is compared against the axisymmetric solution of Eq.(2.6) with no rotation ($\omega = 0$). The
 612 result of the comparison is reported in Figure 8(c) and a good agreement is observed.

613 Figure 9 shows the static cap of the bubble for different inclination angles and Bond
 614 numbers, for same angle $\phi = 0.5^\circ$. For $\alpha < 90^\circ$, the static cap is not axisymmetric: as the tilt
 615 angle increases, the apex of the cap moves toward negative x . Conversely, an elongated region
 616 (tongue) develops in the vicinity of the x axis, in the direction $x > 0$ (i.e. in the direction
 617 of positive gravitational acceleration) and becomes longer as the tilt angle increases. The
 618 elongated region presents abnormal values of mean curvature with respect to the rest of
 619 the cap. The highest (negative) curvature is observed to be localized at the tip point of this
 620 tongue.

621 To obtain the critical conditions, we fix the tilt angle and the Bond number and progressively
 622 decrease the angle ϕ . A preliminary analysis showed that the highest radial curvature is
 623 obtained at the tip point of the tongue (of coordinates $(\bar{x} = 1, \bar{y} = 0)$), in agreement with
 624 the above observations, and increases with decreasing ϕ . For each angle ϕ , we thus compute

625 the radial curvature $\kappa_r = \frac{\partial^2 \bar{h}}{\partial \bar{x}^2} / \left(1 + \left(\frac{\partial \bar{h}}{\partial \bar{x}} \right)^2 \right)^{3/2}$ at the extremity of the tongue. Note that
 626 $\frac{\partial \bar{h}}{\partial \bar{y}}(\bar{x}, \bar{y} = 0) = 0$ because of symmetry. The angle ϕ is then decreased until κ_r vanishes. This
 627 limit value[†] is denoted $\phi_{\lim}(\alpha, Bo)$. For the set of parameters $(Bo, \alpha, \phi = \phi_{\lim}(\alpha, Bo))$, the
 628 liquid-air interface exhibits then an inflection point *at the wall*, and its tangent plane makes
 629 an angle $\phi_{\lim}(\alpha, Bo)$ with the z -direction.

630 Repeating the same procedure varying the Bond number while fixing the tilt angle α ,
 631 we can retrieve ϕ_{\lim} as a function of Bo . In the range $\phi_{\lim} \in [0.5^\circ, 2^\circ]$, $\phi_{\lim}(\alpha, Bo)$ varies
 632 linearly with the Bond number Bo , as shown in Figure 10(a). For each tilt angle α we
 633 interpret the Bond number value at which $\phi_{\lim}(\alpha, Bo_c) = 0$, as the threshold $Bo_c(\alpha)$ for the
 634 onset of motion. We retrieve this value by performing for each tilt angle α , a linear fit of
 635 $\phi_{\lim}(\alpha, Bo)$ for ϕ_{\lim} varying between 0.5° and 2° [‡], and by extrapolating the value $Bo_c(\alpha)$
 636 that corresponds to $\phi_{\lim} = 0^\circ$. The slope of the fit is also a function of α , so that overall,
 637 $\phi_{\lim}(\alpha, Bo)$ is approximated by:

$$638 \quad \phi_{\lim}(\alpha, Bo) = \beta(\alpha) (Bo - Bo_c(\alpha)). \quad (3.8)$$

639 The result of this procedure is displayed on Figure 10. Our study clearly indicates that the
 640 threshold for the onset of motion is lowered by tilting the tube, with a minimum that is
 641 reached for a tilt angle of $45^\circ < \alpha_{\text{opt}} < 50^\circ$. Overall, the critical Bond number and the slope
 642 β as a function of the tilt angle are well approximated by:

$$643 \quad Bo_c(\alpha) \approx 0.54 \left[1 + 0.5 \left(\frac{\pi}{180} \right)^2 (\alpha - 48^\circ)^2 + \left(\frac{\pi}{180} \right)^4 (\alpha - 48^\circ)^4 \right], \quad (3.9)$$

$$644 \quad \beta(\alpha) \approx -\frac{2}{3} \left(\frac{\pi}{180} \right)^2 (\alpha - 51^\circ)^2 + 0.85 \quad [\text{rad.}], \quad (3.10)$$

645 as shown in Figure 10(b). Note that in the vertical case, we retrieved values for the critical
 646 Bond number $Bo_c(\alpha = 90^\circ)$ and for the slope $\beta(\alpha = 90^\circ)$, that match Bretherton's values
 647 ($Bo_c = 0.842$, $\beta = 0.49$ rad.) within 0.03% and 2% of relative error, respectively, thus

[†] The limit value is obtained through linear interpolation, when a change of sign is detected, of the values of curvature between two successive values of ϕ , with a step of 9×10^{-5} rad.

[‡] The fit is performed by considering at least eight points within the declared range. We verified that the threshold and slope do not vary appreciably by decreasing the number of points while keeping a constant distance between the remaining points.

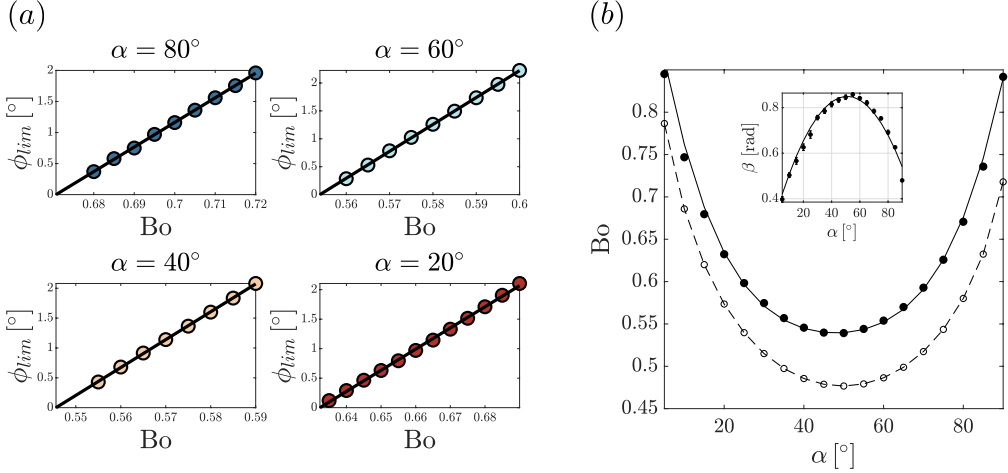


Figure 10: (a) Angle value ϕ_{\lim} for which the radial curvature of the liquid-air interface vanishes at one point at the wall, as a function of Bo for various values of α (colored dots).

For each panel, the black solid line is the linear fit $\phi_{\lim}(\alpha, Bo) = \beta(\alpha) [Bo - Bo_c(\alpha)]$

performed in order to retrieve the threshold for the onset of motion $Bo_c(\alpha)$, that corresponds to $\phi_{\lim} = 0$. (b) Threshold Bo_c as a function of the tilt angle α (black dots). The maximum extrapolation error of the order of 0.001 and is smaller than the marker size. The black solid line represents the polynomial approximation Eq.(3.9). The black circles represent instead the threshold $Bo_c^{2D}(\alpha)$ retrieved from the matching of the thin film with a two-dimensional static cap profile. The black dotted line is a guide for the eyes. (Insert) Coefficient β as a function of the tilt angle α . The errorbars represent the 95% confidence interval. The black solid line represents the polynomial approximation Eq.(3.10)

648 validating further the procedure.

649

650 We now aim at providing a prediction for the ascent velocity. The matching of the two-
651 dimensional thin film region with the static cap shape at the inflection point amounts to
652 enforce:

$$653 \quad 0.572 Bo^{1/3} \sin(\alpha)^{1/3} \left(\frac{b}{R} \right)^{2/3} = \phi_{\lim}(\alpha, Bo) = \beta(\alpha) \left[\frac{\rho g}{\gamma} (R - 1.10b)^2 - Bo_c(\alpha) \right]. \quad (3.11)$$

654 The volume of fluid displaced per unit time by the tip of the bubble $\pi R^2 U_b$ being equal to
655 the volume flux in the uniform film region, $(b/R) = \left(\frac{3Ca}{2Bo \sin(\alpha)} \right)^{1/3}$. Expanding Eq.(3.11) up
656 to first order in (b/R) finally yields the following implicit function for the bubble velocity:

$$657 \quad (Bo - Bo_c(\alpha)) \sin(\alpha) = 2.52 (Bo \sin(\alpha))^{2/3} Ca^{1/3} + \frac{0.63 \sin(\alpha)}{\beta(\alpha)} (Bo \sin(\alpha))^{1/9} Ca^{2/9} \quad (3.12)$$

658 As for the centrifugated case, Eq.(3.12) can be recasted as an equation of the type $x^3 +$
659 $a_1 x^2 + a_2 x + a_3 = 0$, by setting $x = Ca^{1/9}$.

660 3.2. Experiments on tilted bubbles

661 Experimental setup and procedure

662 The same silicone oil used in Section 2.2 is employed to partially fill capillary tubes, that
663 are then sealed on both ends, trapping a long air bubble inside. The inner radii of the
664 tubes vary between 1.08mm and 1.96mm, corresponding to Bond numbers in the range

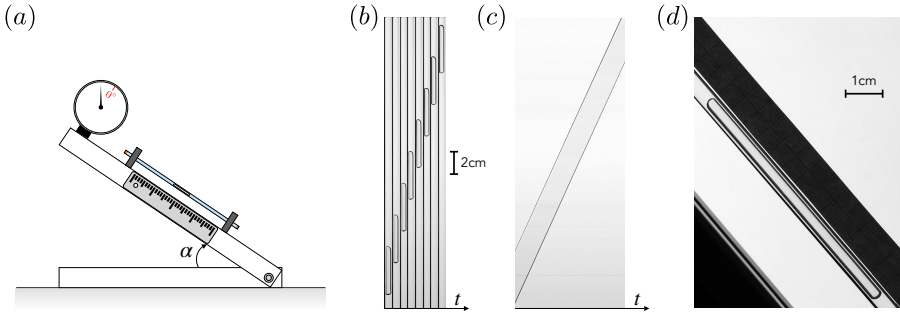


Figure 11: (a) Sketch of the experimental setup. (b) Photographs of a long bubble inside a tube filled with silicone oil, at different and equally spaced time steps. Here, $Bo = 1$ and the tube is tilted by $\alpha = 35^\circ$ with respect to the horizontal axis. (c) Intensity profile as a function of time along the tube axis. To produce this image, a column of pixel aligned with the central axis of the tube is extracted from each frame of the movie. The columns are then juxtaposed to each other. The locations of the upper and lower cap as a function of time are easily identified as the two roughly parallel black curves limiting a slightly darker domain that corresponds to the position of the bubble itself. The rising velocity is given by the slope of these black lines. As in (b), $Bo = 1$ and $\alpha = 35^\circ$. (d) Photograph of a bubble in a tube tilted by $\alpha = 50^\circ$, with $Bo = 0.7$. For these parameters, the system is close to critical conditions for the onset of motion.

665 $Bo \in [0.53, 1.73]$. As in the previous Section, the uncertainty in the tubes inner diameters is
666 of 0.05 mm .

667 The experimental setup is depicted on Figure 11(a). The tube is attached on an aluminium
668 arm that can be tilted by an angle $\alpha \in [0^\circ, 180^\circ]$ with respect to the horizontal plane. A
669 LED panel is positioned behind the setup for visualization purposes. Once the tilt angle is
670 fixed, a camera records the rising motion of the bubble along the central axis of the tube.
671 From the recorded footage, we can then retrieve the bubble velocity as previously described
672 in Section 2.2, and as illustrated in Figure 11(b) and (c). For the narrowest tubes where the
673 bubble velocity is the smallest (if not zero), we use time-lapses instead of movies.

674 Unlike the case of motor-driven rotating tubes, there is in principle no limitation on the
675 observation time, allowing the detection of much slower bubble displacements. In practice,
676 we consider the bubble velocity to be zero if the displacement of the bubble over a week
677 is smaller than our resolution limit of 1mm . This implies that the smallest experimentally
678 measurable capillary number is $Ca_{\min} = 7.6 \times 10^{-9}$.

679 *Experimental results and comparison with the theoretical prediction*

680 Our experimental findings are summarized and compared with our theoretical predictions
681 in Figure 12. Firstly, we observe that the bubble velocity strongly depends on the tilt angle
682 α and reaches its maximum at approximately $\alpha \approx 50^\circ$, a value independent of Bo within
683 the range of Bond numbers investigated here, as shown in Figure 12(b). Furthermore, for
684 $Bo_c(\alpha = 50^\circ) = 0.5401 < Bo < 0.842 = Bo_c(\alpha = 90^\circ)$, tilting the tube by the appropriate
685 angle actually enables the motion of a bubble that would otherwise be stuck in a vertical
686 configuration, as illustrated for instance by the cases $Bo = 0.71$ and $Bo = 0.65$ reported
687 in Figure 12(b). No motion at all is observed below the threshold $Bo_c(\alpha \approx 50^\circ)$. Those
688 observations align well with our theoretical analysis.

689 Finally, the bubble velocity as a function of the tilt angle α at low Bond numbers seems
690 to be well described by Eq.(3.12), without any fitting parameter, see Figure 12(b). We note
691 that the agreement with the theoretical prediction appears to slightly deteriorate at larger
692 Bond numbers. Indeed, several assumptions made in the theoretical analysis, reasonable in

the vicinity of the threshold, are expected to fail in the large Bo regime. Notably, Atasi *et al.* (2017) measured the top and bottom film thickness around long bubbles in horizontal tubes and observed that the film asymmetry grows with the Bond number. Thus, in large capillaries, the thin film thickness cannot be considered as uniform along the azimuthal direction: the lubricating film is indeed much thicker in the direction $x > 0$ (Zukoski 1966). Similarly, requiring the static cap profile to expand in the entire fluid domain $r < R$ is likely to become inadequate as Bo increases. All together however, the comparison tends to validate the relevance of a two-dimensional analysis to describe the thin lubricating film surrounding the bubble, even in a tilted configuration, in the low Bo regime.

It is worth mentioning that as a first attempt to describe the phenomenon, we opted for a fully two-dimensional description of the air-liquid interface. By matching the two-dimensional static cap with the thin film profile, we obtained the threshold $Bc_c^{2D}(\alpha)$ reported in Figure 10(b). This threshold exhibits the same non-monotonic trend as a function of the tilt angle, with a minimum reached for $\alpha_{\text{opt}} \lesssim 50^\circ$. However, it is downward-shifted with respect to the critical Bond number relying on a three-dimensional description of the static cap, which provides a much better agreement with experimental measurements, see Figure 12(a). From this comparison, we conclude that while a simplified, two-dimensional description of the thin film region is acceptable, a proper characterization of the phenomenon requires to account for the three-dimensional shape of the static cap.

712

We can now rationalize the theoretical and experimental results: the increase in transversal acceleration due to the tilt angle tends to increase the film thickness at the tongue of the static cap, enabling higher velocities within the tube for the same axial gravity. However, tilting the tube decreases the driving buoyancy force, which in turn reduces the bubble velocity. The interplay between these two effects leads to the observed non-monotonic dependency of the rising velocity on the tilt angle. In the limit case $\alpha \rightarrow 0^\circ$ (horizontal tube), there is no motion within the tube since the driving force disappears.

713

4. Conclusion

In this study, we investigated theoretically and experimentally two different strategies aimed at enabling the motion of long air bubbles trapped in narrow, sealed capillaries partially filled with a viscous liquid. Both strategies, namely centrifugating the tube or tilting it with respect to its central axis, amount to modify the pressure distribution in the film surrounding the bubble by means of an external force field (centrifugal force or tilted gravity). This impacts both the shape of the static cap of the bubble, and the profile of the liquid-air interface in the thin film region. In particular, the resulting pressure gradients lead in both cases to the thickening of the lubricating film, thus enabling bubble ascent. The threshold for the onset of motion and the rising velocity above threshold as functions of the rotational speed and of tilt angle, respectively, are retrieved by the matching of the static cap and thin film profiles, that conditions the steady ascent of the bubble. Remarkably, the matching conditions in terms of film thickness and slope at the inflection point are in both cases the same as described in Bretherton (1961) for the classical vertical setting (without rotation). However, both centrifugation and inclination alter the inner region solution and the static cap profile, making this matching possible for smaller Bond numbers. Thus, tunable parameters such as the rotational speed or the tilt angle, can effectively lower the threshold for the onset of motion, thus allowing the transport of bubbles even in very narrow capillaries.

The first part of this study was dedicated to the case of a vertical tube in rotation around its central symmetry axis. We extended Bretherton's analysis (Bretherton 1961) to account for the radial pressure gradient resulting from the tube centrifugation. By computing the

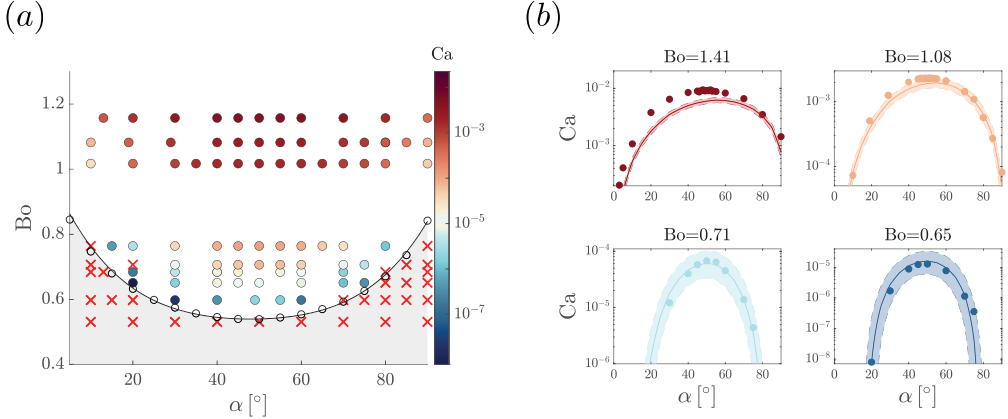


Figure 12: (a) Diagram (Bo, α) where each dot corresponds to a measurement of $Ca > 0$ for a given set of parameters (Bo, α) . The red crosses indicate the couples (Bo, α) for which the bubble displacement fell below our detection limit. The black dots indicate the theoretical threshold for the onset of motion and the black solid line represents the polynomial approximation Eq.(3.9). Below this line, the gray area corresponds to the region of parameters where the steady rising of a bubble is not possible according to our theoretical analysis. (b) Velocity of the bubble as a function of the tilt angle α for various Bond numbers. The dots are the experimental points while for each Bond number, the solid line is described by Eq.(3.12), using the corresponding experimental value of Bo reported in the title of each panel. No fit parameter is used here: the values of $\beta(\alpha)$ and $Bo_c(\alpha)$ in Eq.(3.12) are the ones displayed in Figure 10. The dotted lines also represent the prediction Eq.(3.12), but for $Bo \pm \Delta Bo$, where ΔBo accounts for the ± 0.05 mm uncertainty on the tubes inner diameters. Here, the markers size represents the maximal measurement uncertainty on the bubble velocity.

shape of the tip of the bubble and solving the lubrication equation describing the thin film region, we could derive a matching condition yielding a theoretical prediction for the ascent velocity of the bubble, together with a new threshold for the onset of motion. Our theoretical findings highlight that centrifugating the tube acts as a downward shift on the critical bubble confinement. Our experimental campaign corroborated this analysis and confirmed the relevance of this strategy to release bubbles trapped in very narrow capillaries.

In the second part, we explored how tilting the tube with respect to gravity could influence the transport of the bubble trapped inside. The three-dimensional static cap shape of the bubble was computed numerically, while the thin film region was assumed to be axisymmetric. By matching these profiles at the point of vanishing radial curvature, we could derive a prediction for the steady velocity of the bubble, that can only hold if the inner radius is larger than an angle-dependent critical value. This threshold varies non-monotonically with the tilt angle, with a minimum reached about $\alpha_{\text{opt}} \approx 48^\circ$. Those predictions, although relying on a simplified description of the thin film region, align well with our experimental findings.

Overall, these strategies seem well suited to many microfluidics applications where it is instrumental to get rid of trapped bubbles, without compromising the integrity of the capillary. The use of a tunable external force field provides a practical way to precisely monitor the motion of long bubbles. For further practical uses, we recall here the approximated

760 expressions of the thresholds derived along this study:

$$\text{Bo}_c(\text{Ce}) \approx 0.842 - 0.295 \text{Ce} + 0.020 \text{Ce}^2 \text{ for centrifugated tubes, and:}$$

$$\text{Bo}_c(\alpha) \approx 0.54 \left[1 + 0.5 \left(\frac{\pi}{180} \right)^2 (\alpha - 48^\circ)^2 + \left(\frac{\pi}{180} \right)^4 (\alpha - 48^\circ)^4 \right], \text{ for tilted tubes.}$$

762 At a more fundamental level, these strategies provide an interesting framework to examine
 763 the infinitely slow dynamics of pinch-off, a phenomenon explored theoretically by Lamstaes
 764 & Eggers (2017) and experimentally investigated by Dhaouadi & Kolinski (2019) in capillary
 765 tubes with inner radii $R < R_c$. For instance, starting from a moving bubble within a rotating
 766 capillary and subsequently halting the rotation offers a practical means to establish a precisely
 767 defined initial condition, from which the pinching process starts.

768 Funding

769 We acknowledge the Swiss National Science Foundation under grant 200341.

770 Declaration of Interests

771 The authors report no conflict of interest.

772 Appendix A. Derivation of the thin film velocity profile for the centrifugal and 773 tilted case

774 A.1. Thin film velocity profile in a centrifugated tube

775 Here, we derive the velocity profile in the thin film region when the (vertical) tube is rotated
 776 around its central axis at angular frequency ω . In the rotating reference frame, translating
 777 with the bubble at steady velocity $U_b \mathbf{e}_z$, the stationary Navier-Stokes equations write:

$$\nabla \cdot \mathbf{u} = 0, \quad \rho [(\mathbf{u} \cdot \nabla) \mathbf{u} + 2\boldsymbol{\Omega} \times \mathbf{u}] = -\nabla p - \rho \boldsymbol{\Omega} \times (\boldsymbol{\Omega} \times \mathbf{r}) + \mu \Delta \mathbf{u} + \rho \mathbf{g}, \quad (\text{A } 1)$$

779 where $\boldsymbol{\Omega} = \omega \mathbf{e}_z$ is the rotation vector.

780 We introduce the dimensionless variables $\bar{\mathbf{u}}$, \bar{z} , and \bar{r} , and \bar{p} , such that $\mathbf{u} = U_b \bar{\mathbf{u}}$, $z = R \bar{z}$,
 781 $r = R \bar{r}$ and $p = \pi \bar{p}$, where $\pi = \rho \omega R U_b$. The dimensionless Navier-Stokes equations read:

$$\nabla \cdot \bar{\mathbf{u}} = 0, \quad \text{Ro} (\bar{\mathbf{u}} \cdot \nabla) \bar{\mathbf{u}} + 2\mathbf{e}_z \times \bar{\mathbf{u}} = -\nabla \bar{p} - \frac{1}{\text{Ro}} \mathbf{e}_z \times (\mathbf{e}_z \times \bar{\mathbf{r}}) + E \Delta \bar{\mathbf{u}} - \frac{g}{\omega U_b} \mathbf{e}_z, \quad (\text{A } 2)$$

783 where $\text{Ro} = \frac{U_b}{\omega R}$ is the Rossby number and $E = \frac{\nu}{\omega R^2}$ is the Ekman number. In the experiments
 784 presented in this study, $\text{Ro} \ll 1$ and the non-linear terms of the Navier-Stokes equation can
 785 therefore be neglected. Under these assumptions, and enforcing axisymmetry, the stationary
 786 Navier-Stokes equations in cylindrical coordinates write:

$$0 = \frac{1}{r} \frac{\partial}{\partial r} \left(r u_r \right) + \frac{\partial u_z}{\partial z}, \quad (\text{A } 3)$$

$$-2\rho \omega u_\theta = -\frac{\partial p}{\partial r} + \rho \omega^2 r + \mu \left[\frac{\partial}{\partial r} \left(\frac{1}{r} \frac{\partial}{\partial r} (r u_r) \right) + \frac{\partial^2 u_r}{\partial z^2} \right], \quad (\text{A } 4)$$

$$2\rho \omega u_r = \mu \left[\frac{\partial}{\partial r} \left(\frac{1}{r} \frac{\partial}{\partial r} (r u_\theta) \right) + \frac{\partial^2 u_\theta}{\partial z^2} \right], \quad (\text{A } 5)$$

$$0 = -\frac{\partial p}{\partial z} + \mu \left[\frac{1}{r} \frac{\partial}{\partial r} \left(r \frac{\partial u_z}{\partial r} \right) + \frac{\partial^2 u_z}{\partial z^2} \right] - \rho g. \quad (\text{A } 6)$$

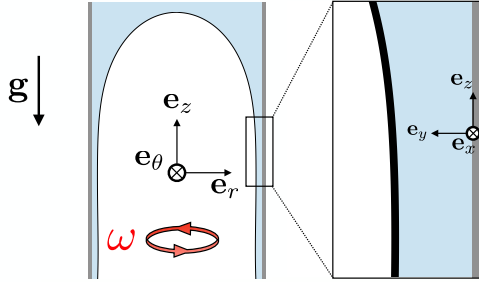


Figure 13: Sketch of the upper part of a long bubble in a sealed vertical tube, rotating around its symmetry axis at angular velocity ω . The flow around the bubble is first described in cylindrical coordinates (r, θ, z) , where e_z is aligned with the tube axis. We focus on the thin film region, that can be considered as planar instead of annular, and describe then the lubricating film in Cartesian coordinates $(x, y = R - r, z)$.

791 Furthermore, in cylindrical coordinates, the stress tensor writes:

$$792 \quad \boldsymbol{\sigma} = \begin{pmatrix} -p + 2\mu \frac{\partial u_r}{\partial r} & \mu r \frac{\partial}{\partial r} \left(\frac{u_\theta}{r} \right) & \mu \left(\frac{\partial u_r}{\partial z} + \frac{\partial u_z}{\partial r} \right) \\ \mu r \frac{\partial}{\partial r} \left(\frac{u_\theta}{r} \right) & -p + \frac{2\mu}{r} u_r & \mu \frac{\partial u_\theta}{\partial z} \\ \mu \left(\frac{\partial u_r}{\partial z} + \frac{\partial u_z}{\partial r} \right) & \mu \frac{\partial u_\theta}{\partial z} & -p + 2\mu \frac{\partial u_z}{\partial z} \end{pmatrix},$$

793 and the vector normal to the interface is $\mathbf{n} = \frac{1}{\sqrt{1+r'_1(z)^2}} (-1, 0, r'_1(z))^T$.

794 Therefore, the dynamic and kinematic boundary conditions at the fluid-air interface are

$$795 \quad \gamma \kappa = (p - p_{\text{air}}) \left(1 + r'_1(z)^2 \right) - 2\mu \left[\frac{\partial u_r}{\partial r} + r'_1(z)^2 \frac{\partial u_z}{\partial z} \right] + 2\mu r'_1(z) \left[\frac{\partial u_r}{\partial z} + \frac{\partial u_z}{\partial r} \right], \quad (\text{A } 7)$$

$$796 \quad 0 = 2r'_1(z) \left[\frac{\partial u_r}{\partial r} - \frac{\partial u_z}{\partial z} \right] + \left(1 - r'_1(z)^2 \right) \left[\frac{\partial u_r}{\partial z} + \frac{\partial u_z}{\partial r} \right], \quad (\text{A } 8)$$

797 where $\kappa = -\frac{1}{r_1(z)\sqrt{1+r'_1(z)^2}} + \frac{r''_1(z)}{(1+r'_1(z)^2)^{3/2}}$ is the curvature.

798 Finally, the no-slip boundary condition at the solid wall implies $u_z(r = R) = -U_b$.

799 Change of coordinates

800 In the thin film region, the film thickness is very small compared to the radius, so that the
 801 flow can be treated as if the region were planar, instead of annular. Accordingly, we describe
 802 the flow in the Cartesian coordinate system $(x, y = R - r, z)$, see Figure 13. Furthermore, we
 803 introduce the modified pressure field: $P = p + \rho\omega^2 Ry + \rho g z$. In this system of coordinates,
 804 the Navier-Stokes equation become:

829 constraint $\rho g b^3 / 3\mu U_b = R/2$, we deduce that $\frac{C_a}{C_e} \sim \epsilon^3 \frac{2g}{3\omega^2 R} = O(\epsilon^3)$. Thus, the system of
830 equations reduces to:

$$831 \quad 0 = \frac{\partial \bar{u}_y}{\partial \bar{y}} + \frac{\partial \bar{u}_z}{\partial \bar{z}}, \quad 0 = \frac{\partial \bar{P}}{\partial \bar{y}}, \quad 0 = -\frac{\partial \bar{P}}{\partial \bar{z}} + \frac{\partial^2 \bar{u}_z}{\partial \bar{y}^2}. \quad (\text{A 19})$$

832 The dynamic and kinematic boundary conditions are:

$$833 \quad \gamma\kappa = \frac{\mu U_b}{b\epsilon} \left(\bar{P} - \bar{P}_{\text{air}} \right) \left(1 + \epsilon^2 \bar{y}_1'(\bar{z})^2 \right) - 2\epsilon \frac{\mu U_b}{b} \left[\frac{\partial \bar{u}_y}{\partial \bar{y}} + \epsilon^2 \bar{y}_1'(\bar{z})^2 \frac{\partial \bar{u}_z}{\partial \bar{z}} \right] \\ 834 \quad + 2\epsilon \frac{\mu U_b}{b} \bar{y}_1'(\bar{z}) \left[\epsilon^2 \frac{\partial \bar{u}_y}{\partial \bar{z}} + \frac{\partial \bar{u}_z}{\partial \bar{y}} \right], \quad (\text{A 20})$$

$$835 \quad 0 = 2\epsilon^2 \bar{y}_1'(\bar{z}) \left[\frac{\partial \bar{u}_y}{\partial \bar{y}} - \frac{\partial \bar{u}_z}{\partial \bar{z}} \right] + \left(1 - \epsilon^2 \bar{y}_1'(\bar{z})^2 \right) \left[\epsilon^2 \frac{\partial \bar{u}_y}{\partial \bar{z}} + \frac{\partial \bar{u}_z}{\partial \bar{y}} \right]. \quad (\text{A 21})$$

836 Thus, including the no-slip boundary condition at the solid wall, the boundary conditions
837 at leading order are:

$$838 \quad \bar{P} - \bar{P}_{\text{air}} = \gamma\kappa \frac{\epsilon b}{\mu U_b}, \quad \frac{\partial \bar{u}_z}{\partial \bar{y}} = 0, \quad \bar{u}_z(\bar{y} = 0) = -1. \quad (\text{A 22})$$

839 Finally, going back to the dimensional form, and reintroducing the original pressure field
840 $p = P - \rho\omega^2 Ry - \rho gz$, the full problem writes:

$$841 \quad 0 = \frac{\partial u_y}{\partial y} + \frac{\partial u_z}{\partial z}, \quad \frac{\partial p}{\partial y} = -\rho\omega^2 R, \quad \frac{\partial p}{\partial z} = \mu \frac{\partial^2 u_z}{\partial y^2} - \rho g, \quad (\text{A 23})$$

842 and is complemented by the following boundary conditions:

$$843 \quad p(y = y_1, z) - p_{\text{air}} = \gamma\kappa, \quad \frac{\partial u_z}{\partial y}|_{y=y_1} = 0, \quad u_z(y = 0, z) = -U_b. \quad (\text{A 24})$$

844 The integration of the pressure field is straightforward and leads to:

$$845 \quad p(y, z) = p_{\text{air}} + \gamma\kappa + \rho\omega^2 R (y_1(z) - y). \quad (\text{A 25})$$

846 Finally, by injecting this pressure field in the axial component of the momentum equation,
847 we can derive the following equation for the velocity in the thin film:

$$848 \quad \mu \frac{\partial^2 u_z}{\partial y^2} = \gamma\kappa' + \rho\omega^2 R y'_1 + \rho g, \quad (\text{A 26})$$

849 that results into:

$$850 \quad u_z(y, z) = -U_b + \frac{\gamma}{2\mu} \left(\kappa' + \frac{\rho\omega^2 R}{\gamma} y'_1 + \frac{\rho g}{\gamma} \right) (y^2 - 2y_1 y). \quad (\text{A 27})$$

A.2. Thin film velocity profile in a tilted tube

851 We now aim at deriving the velocity profile in the thin film region when the tube is tilted by
852 an angle α . Since the Reynolds number $\text{Re} = \rho U_b b / \mu$ characterizing the flow in the thin film
853 region is very small, we can safely neglect the effect of inertia. In the stationary cylindrical
854 system of coordinates (r, θ, z) , translating with the bubble at steady velocity $U_b \mathbf{e}_z$ where z is
855 aligned with the central axis of the (tilted) tube, see Figure 14(a), the Navier-Stokes equation
856 read:
857

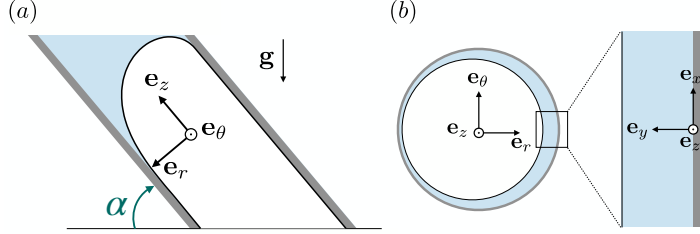


Figure 14: (a) Sketch of the upper part of a long bubble in a sealed tube tilted by an angle α with respect to the horizontal plane. The flow in the thin lubricating film is described in cylindrical coordinates (r, θ, z) , where \mathbf{e}_z is the direction aligned with the tube axis, such that $\mathbf{e}_z \cdot \mathbf{g} = -g \sin(\alpha)$. The origin of θ is chosen such that $\mathbf{e}_r(\theta = 0) \cdot \mathbf{g} = g \cos(\alpha)$. (b) Sketch of the cross-section of the channel and of the bubble. We focus on the region in the vicinity of the plane $\theta = 0$, described in Cartesian coordinates $(x, y = R - r, z)$, where $\mathbf{e}_x \cdot \mathbf{g} = 0$, $\mathbf{e}_y \cdot \mathbf{g} = -g \cos(\alpha)$, and $\mathbf{e}_z \cdot \mathbf{g} = -g \sin(\alpha)$.

858 $0 = \frac{1}{r} \frac{\partial}{\partial r} \left(r u_r \right) + \frac{1}{r} \frac{\partial u_\theta}{\partial \theta} + \frac{\partial u_z}{\partial z}, \quad (\text{A } 28)$

859 $0 = -\frac{\partial p}{\partial r} + \mu \left[\frac{\partial}{\partial r} \left(\frac{1}{r} \frac{\partial}{\partial r} (r u_r) \right) + \frac{1}{r^2} \frac{\partial^2 u_r}{\partial \theta^2} - \frac{2}{r^2} \frac{\partial u_\theta}{\partial \theta} + \frac{\partial^2 u_r}{\partial z^2} \right] + \rho g \cos(\theta) \cos(\alpha), \quad (\text{A } 29)$

860 $0 = -\frac{\partial p}{\partial \theta} + \mu \left[\frac{\partial}{\partial r} \left(\frac{1}{r} \frac{\partial}{\partial r} (r u_\theta) \right) + \frac{1}{r^2} \frac{\partial^2 u_\theta}{\partial \theta^2} + \frac{2}{r^2} \frac{\partial u_r}{\partial \theta} + \frac{\partial^2 u_\theta}{\partial z^2} \right] - \rho g \sin(\theta) \cos(\alpha), \quad (\text{A } 30)$

861 $0 = -\frac{\partial p}{\partial z} + \mu \left[\frac{1}{r} \frac{\partial}{\partial r} \left(r \frac{\partial u_z}{\partial r} \right) + \frac{1}{r^2} \frac{\partial^2 u_z}{\partial \theta^2} + \frac{\partial^2 u_z}{\partial z^2} \right] - \rho g \sin(\alpha). \quad (\text{A } 31)$

862 We know from our analysis of the three-dimensional cap profile, that the matching with
863 the thin film region profile should be imposed at the tip of the tongue exhibited by the static
864 cap, i.e. at the point of coordinates $(r = R, \theta = 0, h(R, 0))$. We will thus restrict the study
865 of the thin film solution to the plane $(\theta = 0)$, see Figure 14(b). By assuming a vanishing
866 azimuthal curvature $\sim 1/R$, the region of size $\sim Rd\theta$ in the close vicinity of $\theta = 0$ can be
867 considered infinite. Yet, in the vicinity of $\theta = 0$, the derivative with respect to θ should vanish
868 by symmetry. Therefore, in this region, the Navier-Stokes equations reduce to:

869 $0 = \frac{1}{r} \frac{\partial}{\partial r} \left(r u_r \right) + \frac{\partial u_z}{\partial z}, \quad (\text{A } 32)$

870 $0 = -\frac{\partial p}{\partial r} + \mu \left[\frac{\partial}{\partial r} \left(\frac{1}{r} \frac{\partial}{\partial r} (r u_r) \right) + \frac{\partial^2 u_r}{\partial z^2} \right] + \rho g \cos(\alpha), \quad (\text{A } 33)$

871 $0 = \mu \left[\frac{\partial}{\partial r} \left(\frac{1}{r} \frac{\partial}{\partial r} (r u_\theta) \right) + \frac{\partial^2 u_\theta}{\partial z^2} \right], \quad (\text{A } 34)$

872 $0 = -\frac{\partial p}{\partial z} + \mu \left[\frac{1}{r} \frac{\partial}{\partial r} \left(r \frac{\partial u_z}{\partial r} \right) + \frac{\partial^2 u_z}{\partial z^2} \right] - \rho g \sin(\alpha). \quad (\text{A } 35)$

873 These equations are complemented by the following dynamic and kinematic boundary

874 conditions:

$$875 \quad \gamma\kappa = (p - p_{\text{air}}) \left(1 + r'_1(z)^2\right) - 2\mu \left[\frac{\partial u_r}{\partial r} + r'_1(z)^2 \frac{\partial u_z}{\partial z} \right] + 2\mu r'_1(z) \left[\frac{\partial u_r}{\partial z} + \frac{\partial u_z}{\partial r} \right], \quad (\text{A } 36)$$

$$876 \quad 0 = 2r'_1(z) \left[\frac{\partial u_r}{\partial r} - \frac{\partial u_z}{\partial z} \right] + \left(1 - r'_1(z)^2\right) \left[\frac{\partial u_r}{\partial z} + \frac{\partial u_z}{\partial r} \right], \quad (\text{A } 37)$$

877 where $\kappa = -\frac{1}{r_1(z)\sqrt{1+r'_1(z)^2}} + \frac{r''_1(z)}{(1+r'_1(z)^2)^{3/2}}$ is the curvature, and by the no-slip boundary
878 condition at the solid wall: $u_z(r = R) = -U_b$.

879 Change of coordinates

880 As before, we neglect curvature in the azimuthal direction, and describe the thin film region
881 within the Cartesian coordinate system $(x, y = R - r, z)$, see Figure 14(b). Furthermore, we
882 introduce the modified pressure field: $P = p + \rho g \cos(\alpha)y + \rho g \sin(\alpha)z$. In this system of
883 coordinates, the mass conservation and momentum conservation equations along the y and
884 z directions become:

$$885 \quad 0 = \frac{\partial u_y}{\partial y} + \frac{\partial u_z}{\partial z} - \frac{u_y}{R - y},$$

$$886 \quad 0 = \frac{\partial P}{\partial y} + \mu \left[\frac{1}{R - y} \frac{\partial u_y}{\partial y} + \frac{u_y}{(R - y)^2} - \frac{\partial^2 u_y}{\partial y^2} - \frac{\partial^2 u_y}{\partial z^2} \right],$$

$$887 \quad 0 = -\frac{\partial P}{\partial z} + \mu \left[-\frac{1}{R - y} \frac{\partial u_z}{\partial y} + \frac{\partial^2 u_z}{\partial y^2} + \frac{\partial^2 u_z}{\partial z^2} \right].$$

888 Likewise, the dynamic and kinematic boundary conditions become:

$$889 \quad \gamma\kappa = (P - P_{\text{air}}) \left(1 + y'_1(z)^2\right) - 2\mu \left[\frac{\partial u_y}{\partial y} + y'_1(z)^2 \frac{\partial u_z}{\partial z} \right] + 2\mu y'_1(z) \left[\frac{\partial u_y}{\partial z} + \frac{\partial u_z}{\partial y} \right], \quad (\text{A } 38)$$

$$890 \quad 0 = 2y'_1(z) \left[\frac{\partial u_y}{\partial y} - \frac{\partial u_z}{\partial z} \right] + \left(1 - y'_1(z)^2\right) \left[\frac{\partial u_y}{\partial z} + \frac{\partial u_z}{\partial y} \right], \quad (\text{A } 39)$$

891 where $\kappa = -\frac{1}{(R - y_1(z))\sqrt{1+y'_1(z)^2}} - \frac{y''_1(z)}{(1+y'_1(z)^2)^{3/2}}$.

892 Lubrication approximation

893 We nondimensionalize as follows: $u_z = U_b \bar{u}_z$, $u_y = U_y \bar{u}_y$, $P = P_0 \bar{P}$, $y = b \bar{y}$, $y_1 = b \bar{y}_1$,
894 $z = R \bar{z}$, where $\epsilon = \frac{b}{R} \ll 1$. According to the least degeneracy principle applied to the mass
895 conservation equation, $U_y = \epsilon U_b$ and the mass conservation equation becomes: $0 = \frac{\partial \bar{u}_y}{\partial \bar{y}} + \frac{\partial \bar{u}_z}{\partial \bar{z}}$.

896 Furthermore, upon introduction of the dimensionless fields and variables, the momentum
897 conservation equations along the y and z directions are written as:

$$898 \quad 0 = \frac{P_0}{b} \frac{\partial \bar{P}}{\partial \bar{y}} + \frac{\epsilon \mu U_b}{b^2} \left[\frac{\epsilon}{1 - \epsilon \bar{y}} \frac{\partial \bar{u}_y}{\partial \bar{y}} + \frac{\epsilon^2}{(1 - \epsilon \bar{y})^2} \bar{u}_y - \frac{\partial^2 \bar{u}_y}{\partial \bar{y}^2} - \epsilon^2 \frac{\partial^2 \bar{u}_y}{\partial \bar{z}^2} \right], \quad (\text{A } 40)$$

$$899 \quad 0 = -\frac{P_0}{R} \frac{\partial \bar{P}}{\partial \bar{z}} + \frac{\mu U_b}{b^2} \left[-\frac{\epsilon}{1 - \epsilon \bar{y}} \frac{\partial \bar{u}_z}{\partial \bar{y}} + \frac{\partial^2 \bar{u}_z}{\partial \bar{y}^2} + \epsilon^2 \frac{\partial^2 \bar{u}_z}{\partial \bar{z}^2} \right]. \quad (\text{A } 41)$$

900 The least degeneracy principle applied to the momentum conservation equation along the

901 z -axis implies that: $P_0 = \frac{\mu U_b}{b\epsilon}$. At leading order, the problem reduces then to:

$$902 \quad 0 = \frac{\partial \bar{u}_y}{\partial \bar{y}} + \frac{\partial \bar{u}_z}{\partial \bar{z}}, \quad 0 = \frac{\partial \bar{P}}{\partial \bar{y}}, \quad 0 = -\frac{\partial \bar{P}}{\partial \bar{z}} + \frac{\partial^2 \bar{u}_z}{\partial \bar{y}^2}. \quad (\text{A 42})$$

903 The dynamic and kinematic boundary conditions are:

$$904 \quad \gamma\kappa = \frac{\mu U_b}{b\epsilon} \left(\bar{P} - \bar{P}_{\text{air}} \right) \left(1 + \epsilon^2 \bar{y}_1'(\bar{z})^2 \right) - 2\epsilon \frac{\mu U_b}{b} \left[\frac{\partial \bar{u}_y}{\partial \bar{y}} + \epsilon^2 \bar{y}_1'(\bar{z})^2 \frac{\partial \bar{u}_z}{\partial \bar{z}} \right] \\ 905 \quad + 2\epsilon \frac{\mu U_b}{b} \bar{y}_1'(\bar{z}) \left[\epsilon^2 \frac{\partial \bar{u}_y}{\partial \bar{z}} + \frac{\partial \bar{u}_z}{\partial \bar{y}} \right], \quad (\text{A 43})$$

$$906 \quad 0 = 2\epsilon^2 \bar{y}_1'(\bar{z}) \left[\frac{\partial \bar{u}_y}{\partial \bar{y}} - \frac{\partial \bar{u}_z}{\partial \bar{z}} \right] + \left(1 - \epsilon^2 \bar{y}_1'(\bar{z})^2 \right) \left[\epsilon^2 \frac{\partial \bar{u}_y}{\partial \bar{z}} + \frac{\partial \bar{u}_z}{\partial \bar{y}} \right]. \quad (\text{A 44})$$

907 Therefore at leading order, and including the no-slip boundary condition at the solid wall,
908 the boundary conditions write:

$$909 \quad \bar{P} - \bar{P}_{\text{air}} = \gamma\kappa \frac{\epsilon b}{\mu U_b}, \quad \frac{\partial \bar{u}_z}{\partial \bar{y}} = 0, \quad \bar{u}_z(\bar{y} = 0) = -1. \quad (\text{A 45})$$

910 Finally, going back to the dimensional form, and reintroducing the original pressure field
911 $p = P - \rho g \cos(\alpha)y - \rho g \sin(\alpha)z$, the full problem reduces to:

$$912 \quad 0 = \frac{\partial u_y}{\partial y} + \frac{\partial u_z}{\partial z}, \quad \frac{\partial p}{\partial y} = -\rho g \cos(\alpha), \quad \frac{\partial p}{\partial z} = \mu \frac{\partial^2 u_z}{\partial y^2} - \rho g \sin(\alpha), \quad (\text{A 46})$$

913 and is complemented by the following boundary conditions:

$$914 \quad p(y = y_1, z) - p_{\text{air}} = \gamma\kappa, \quad \frac{\partial u_z}{\partial y}|_{y=y_1} = 0, \quad u_z(y = 0, z) = -U_b. \quad (\text{A 47})$$

915 The pressure field integrates straightforwardly into:

$$916 \quad p(y, z) = p_{\text{air}} + \gamma\kappa + \rho g \cos(\alpha) (y_1(z) - y). \quad (\text{A 48})$$

917 Finally, by injecting this pressure field in the axial component of the momentum equation,
918 we can derive the following equation for the velocity in the thin film:

$$919 \quad \mu \frac{\partial^2 u_z}{\partial y^2} = \gamma\kappa' + \rho g \cos(\alpha) y'_1 + \rho g \sin(\alpha), \quad (\text{A 49})$$

920 which leads to the velocity profile:

$$921 \quad u_z(y, z) = -U_b + \frac{\gamma}{2\mu} \left(\kappa' + \frac{\rho g \cos(\alpha)}{\gamma} y'_1 + \frac{\rho g \sin(\alpha)}{\gamma} \right) (y^2 - 2y_1 y). \quad (\text{A 50})$$

922 Appendix B. Derivation of the equilibrium equation for the static cap

923 Following previous works (see e.g. Rascón & Aarts (2017); Lubbers *et al.* (2014); Manning
924 *et al.* (2011)), we derive from energy principles the three-dimensional equilibrium equation
925 for the equilibrium of the static cap. We introduce the coordinate system (x, y, z) , with the
926 z axis aligned with the central tube axis, and the x axis aligned with the gravity component
927 normal to the z axis (so that $\mathbf{e}_x \cdot \mathbf{g} = g \cos(\alpha)$, see Figure 8(a)). The location of the air-liquid
928 interface is denoted by $h(x, y)$.

929 The Gibbs free energy associated with the cap interface can be written as:

$$930 \quad E(h) = \gamma \mathcal{A} + \mathcal{G}, \quad (\text{B } 1)$$

931 where the first term on the right-hand-side is the surface energy. As in Rascón & Aarts
932 (2017), the surface \mathcal{A} is computed as

$$933 \quad \mathcal{A} = \int_{\Omega} \sqrt{1 + (\nabla h)^2} dx dy, \quad (\text{B } 2)$$

934 with Ω the cross-section of the capillary. The term \mathcal{G} represents in turn the gravitational
935 potential energy, that in general form reads (Pitts 1973):

$$936 \quad \mathcal{G} = - \int_V \rho \mathbf{g} \cdot \mathbf{r} dx dy dz, \quad \mathbf{r} = (x, y, z), \quad \mathbf{g} = g(\cos \alpha, 0, -\sin \alpha), \quad (\text{B } 3)$$

937 where the volume V is given by:

$$938 \quad V = \int_{\Omega} dx dy h(x, y). \quad (\text{B } 4)$$

939 Upon introduction of the Lagrange multiplier λ to ensure volume conservation, the functional
940 to be minimized to obtain equilibrium reads:

$$941 \quad F(h) = \gamma \int_{\Omega} \sqrt{1 + (\nabla h)^2} dx dy + \rho g \int_V (-x \cos \alpha + z \sin \alpha) dx dy dz - \lambda \int_{\Omega} h dx dy. \quad (\text{B } 5)$$

942 Upon integration along the z direction between 0 and h :

$$943 \quad F(h) = \gamma \int_{\Omega} \sqrt{1 + (\nabla h)^2} dx dy + \rho g \int_{\Omega} \left(-x \cos \alpha + \frac{1}{2} h \sin \alpha \right) h dx dy - \lambda \int_{\Omega} h dx dy. \quad (\text{B } 6)$$

944 Formal minimization of the functional $F(h)$ with respect to h leads to the following partial
945 differential equation:

$$946 \quad \gamma \nabla \cdot \left(\frac{\nabla h}{\sqrt{1 + (\nabla h)^2}} \right) = \rho g (\cos(\alpha)x - h \sin(\alpha)) + \lambda, \quad (\text{B } 7)$$

947 with the constant slope condition at the wall:

$$948 \quad \frac{\nabla h}{\sqrt{1 + (\nabla h)^2}} \cdot \mathbf{n} = -\cos(\phi), \quad (\text{B } 8)$$

949 where \mathbf{n} is the unit exterior normal to the tube wall. The value of λ can be set by integrating the
950 resulting equilibrium equation within the whole domain, leading to the following expression:

$$951 \quad \lambda = -\frac{2\gamma}{R} \cos(\phi) + \rho g h_0 \sin \alpha, \quad (\text{B } 9)$$

952 where $h_0 = V/\Omega$ is the reference average value of the static cap height. By imposing $\lambda = 0$,
953 the reference height reads $h_0 = \frac{2\ell_c^2 \cos(\phi)}{R \sin \alpha}$, reminiscent of the well-known Jurin height. Upon
954 non-dimensionalization with the tube radius R , one obtains the equilibrium equation reported
955 in the main text Eq.(3.1).

REFERENCES

956 ACRIVOS, A. & HERBOLZHEIMER, E. 1979 Enhanced sedimentation in settling tanks with inclined walls. *J.*
957 *Fluid Mech.* **92**, 435–457.

- 958 ATASI, O., KHODAPARAST, S., SCHEID, B. & STONE, H. A. 2017 Effect of buoyancy on the motion of long
959 bubbles in horizontal tubes. *Phys. Rev. Fluids* **2**, 094304.
- 960 BAROUD, C.N., GALLAIRE, F. & DANGLA, R. 2010 Dynamics of microfluidic droplets. *Lab on a Chip* **10**,
961 2032–2045.
- 962 BAROUD, C. N., DE SAINT VINCENT, M. R. & DELVILLE, J.-P. 2007 An optical toolbox for total control of
963 droplet microfluidics. *Lab on a Chip* **7**, 1029–1033.
- 964 BENDIKSEN, K.H. 1984 An experimental investigation of the motion of long bubbles in inclined tubes. *Int.
965 J. Multiph. Flow* **10**, 467–483.
- 966 BI, Q.C. & ZHAO, T.S. 2001 Taylor bubbles in miniaturized circular and noncircular channels. *Intl J.
967 Multiphase Flow* **27**, 561–570.
- 968 BICO, J. & QUÉRÉ, D. 2002 Rise of liquids and bubbles in angular capillary tubes. *J. Colloid Interface Sci.
969* **247**, 162–166.
- 970 BICO, J., TORDEUX, C. & QUÉRÉ, D. 2001 Rough wetting. *EPL* **55**, 214.
- 971 BOUCHER, A., KARP, J., BELT, R. & LINÉ, A. 2023 Dynamics of elongated bubbles in slightly inclined pipes
972 with viscous fluids. *J. Fluid Mech.* **977**, A40.
- 973 BOYCOTT, A.E. 1920 Sedimentation of blood corpuscles. *Nature* **104**, 532–532.
- 974 BRANNOCK, D. & KUBIE, J. 1996 Velocity of long bubbles in oscillating vertical pipes. *Intl J. Multiphase
975 Flow* **22**, 1031–1034.
- 976 BRETHERTON, F.P. 1961 The motion of long bubbles in tubes. *J. Fluid Mech.* **10**, 166–188.
- 977 BRODRIBB, T.J., BIENAIMÉ, D. & MARMOTTANT, P. 2016 Revealing catastrophic failure of leaf networks
978 under stress. *Proc. Nat. Acad. Sci. USA* **113**, 4865–4869.
- 979 CHENG, H.B. & LU, Y.W. 2014 Applications of textured surfaces on bubble trapping and degassing for
980 microfluidic devices. *Microfluid. Nanofluid.* **15**, 855–862.
- 981 COLLICOTT, S.H. & MANNING, R.E. 2014 Capillary stability in a tilted circular cylinder. *Microgravity Sci.
982 Technol.* **25**, 319–326.
- 983 CORAPCIOGLU, M. Y., CIHAN, A. & DRAZENOVIC, M. 2004 Rise velocity of an air bubble in porous media:
984 Theoretical studies. *Water Resour. Res.* **40**, W04214.
- 985 COUËT, B. & STRUMOLO, G.S. 1987 The effects of surface tension and tube inclination on a two-dimensional
986 rising bubble. *J. Fluid Mech.* **184**, 1–14.
- 987 DAVIES, R.M. & TAYLOR, G.I. 1950 The mechanics of large bubbles rising through extended liquids and
988 through liquids in tubes. *Proc. R. Soc. Lond. A* **200**, 375–390.
- 989 DHAOUADI, W. & KOLINSKI, J.M. 2019 Bretherton's buoyant bubble. *Phys. Rev. Fluids* **4**, 123601.
- 990 DRELICH, J., FANG, C. & WHITE, C.L. 2002 Measurement of interfacial tension in fluid-fluid systems.
991 *Encyclopedia of surface and colloid science* **3**, 3158–3163.
- 992 DUMITRESCU, D.T. 1943 Strömung an einer luftblase im senkrechten rohr. *J. Appl. Math. Mech./Z. Angew.
993 Math. Mech.* **23** (3), 139–149.
- 994 EMSLIE, A.G., BONNER, F.T. & PECK, L.G. 1958 Flow of a viscous liquid on a rotating disk. *Journal of
995 Applied Physics* **29** (5), 858–862.
- 996 FAIRBROTHER, F. & STUBBS, A. E. 1935 Studies in electro-endosmosis. part vi. the “bubble-tube” method
997 of measurement. *J. Chem. Soc.* **1**, 527–529.
- 998 FUNADA, T., JOSEPH, D.D., MAEHARA, T. & YAMASHITA, S. 2005 Ellipsoidal model of the rise of a taylor
999 bubble in a round tube. *Intl J. Multiphase Flow* **31**, 473–491.
- 1000 GARY, J. H., HANDWERK, J. H., KAISER, M. J. & GEDDES, D. 2007 *Petroleum refining: technology and
1001 economics*. CRC press.
- 1002 GIBSON, A.H. 1913 On the motion of long air-bubbles in a vertical tube. *Lond. Edinb. Phil. Mag.* **26**,
1003 952–965.
- 1004 GROELL, R., SCHAFFLER, G. J. & RIENMUELLER, R. 1997 The peripheral intravenous cannula: a cause of
1005 venous air embolism. *The American journal of the medical sciences* **314**, 300–302.
- 1006 GUO, L., LIU, Y. & RAN, P. ET AL. 2022 A bioinspired bubble removal method in microchannels based on
1007 angiosperm xylem embolism repair. *Microsyst. Nanoeng.* **8**, 34.
- 1008 JAMBON-PUILLET, E., ROYER PIÉCHAUD, M. & BRUN, P.-T. 2021 Elastic amplification of the rayleigh-
1009 taylor instability in solidifying melts. *Proceedings of the National Academy of Sciences* **118** (10),
1010 e2020701118.
- 1011 JENSEN, M.J., GORANOVIĆ, G. & BRUUS, H. 2004 The clogging pressure of bubbles in hydrophilic
1012 microchannel contractions. *J. Micromech. Microeng.* **14**, 876.

- 1070 WANG, S. & CLARENS, A.F. 2012 The effects of co₂-brine rheology on leakage processes in geologic carbon
1071 sequestration. *Water Resour. Res.* **48**, W08518.
- 1072 WEBER, M.E., ALARIE, A. & RYAN, M.E. 1986 Velocities of extended bubbles in inclined tubes. *Chem. Eng. Sci.* **41**, 2235–2240.
- 1074 WHITE, E.T. & BEARDMORE, R.H. 1962 The velocity of rise of single cylindrical air bubbles through liquids
1075 contained in vertical tubes. *Chem. Eng. Sci.* **17**, 351–361.
- 1076 YU, Y.E., KHODAPARAST, S. & STONE, H.A. 2018 Separation of particles by size from a suspension using
1077 the motion of a confined bubble. *Appl. Phys. Lett.* **112**, 181604.
- 1078 YU, Y.E., MAGNINI, M., ZHU, L., SHIM, S. & STONE, H.A. 2021 Non-unique bubble dynamics in a vertical
1079 capillary with an external flow. *J. Fluid Mech.* **911**, A34.
- 1080 YUAN, Y., GIRI, G., AYZNER, A.L., ZOOMBELT, A.P., MANNSFELD, S.C.B., CHEN, J., NORDLUND, D., TONEY,
1081 M.F., HUANG, J & BAO, Z. 2014 Ultra-high mobility transparent organic thin film transistors grown
1082 by an off-centre spin-coating method. *Nature communications* **5** (1), 3005.
- 1083 ZHOU, G. & PROSPERETTI, A. 2021 Faster taylor bubbles. *J. Fluid Mech.* **920**, R2.
- 1084 ZHOU, G. & PROSPERETTI, A. 2024 Volume oscillations slow down a rising taylor bubble. *J. Fluid Mech.*
1085 **978**, A13.
- 1086 ZUKOSKI, E.E. 1966 Influence of viscosity, surface tension, and inclination angle on motion of long bubbles
1087 in closed tubes. *J. Fluid Mech.* **25**, 821–837.